Materials Advances

ROYAL SOCIETY OF CHEMISTRY

REVIEW

View Article Online
View Journal | View Issue

Cite this: *Mater. Adv.*, 2025, **6**, 13

Exciton binding energies and polaron interplay in the optically excited state of organic–inorganic lead halide perovskites

Zeeshan Muhammad *[a] and Arooj Rashid[b]

Organic–inorganic lead halide perovskites (OILHPs) have been spotlighted by many researchers due to their unique features and potential for high-performance devices. One of the major obstacles with perovskites is determining the universal value for the exciton binding energy. Numerous contradictory reports in previous studies reveal a wide range of values for the exciton binding energy, spanning from a few meV to several hundred meV. Here we review different experimental and theoretical methodologies carried out to measure the exciton binding energy of OILHPs. Some of the recently explored parameters in the literature that influence exciton binding energy, like exciton dynamics and recombination, are also discussed. Besides this, prospective research initiatives in the field of exciton binding energies, with an emphasis on improving measurement precision and understanding exciton–polaron dynamics, are also highlighted. This critical understanding of exciton and polaron physics is a significant resource for researchers working on exciton-related phenomena, allowing for future breakthroughs in the design and development of efficient, high-performance devices.

Received 1st May 2024,
Accepted 14th October 2024

DOI: 10.1039/d4ma00454j

rsc.li/materials-advances

1 Introduction

Organic–inorganic lead halide perovskites (OILHPs) are characterized by the general chemical expression of $APbX_3$, where A represents cation groups such as methylammonium (MA; CH_3NH_3), formamidinium (FA; $CH(NH_2)_2$), cesium (Cs) or their mixtures, and X represents a halide like iodide (I), bromide (Br), chloride (Cl), or their mixed composition. Such materials have proven remarkable electronic and optical properties, making them promising for high-efficiency, low-cost devices. Some of the notable features of these materials that render them exceptional are their band gap tailoring for optimum solar absorption,[1–7] enhanced carrier lifetimes,[1,8,9] long charge carrier diffusion length,[9–11] high charge carrier mobility,[10,12–14] and abnormally high defect tolerance.[15–17] Research on amplified spontaneous emission (ASE) or lasers,[18–22] light-emitting diodes (LEDs),[23–25] and photodetectors[26–34] has attracted significant interest in the aftermath of OILHPs' success in photovoltaics[35–43] thereby replacing the traditional III–V compound semiconductors. Meanwhile, the rapid advancement of OILHPs across various applications has led to a growing interest in understanding their photophysical properties to explain the origins of their exceptional device performance and the nature of the photoexcitation species that are widely discussed.[38,44–48]

In most of the studies, it has been shown that in OILHPs, the optical excitation close to the bandgap impacts the main factors, like hampering the bound state of e–h pairs and their transport behavior, which in turn affects the performance of photovoltaic and optoelectronic devices. The consideration of e–h coulombic interactions usually refers to excitons during excitation. The amount of energy required to hold or break up such bound states of photoexcited e–h pairs is known as exciton binding energy (E_{xb}), which is helpful in explaining the fundamentals of photophysics and their connection to device performances. Understanding the exciton binding energy offers insights for optimizing OILHP-based devices, leading to enhanced performance. In a typical direct bandgap semiconducting material, two types of optically excited states occur near the band edge: free charge carriers and excitons. Generally, inorganic semiconductors, like GaAs, GaN, and InP, are usually considered free carrier materials, with their excited levels mainly dominated by free carriers as excitons known as Wannier–Mott excitons, which dissociate instantaneously into free carriers upon photoexcitation. Such materials have small effective masses and high permittivity, and their exciton binding energy is lower (less than 10 meV) in comparison to thermal energy (k_BT) at room temperature (RT).[49,50] On the other hand, bulk organic semiconductors, such as molecular crystals, are excitonic materials because their excited states are primarily

[a] *Department of Physics, International Islamic University, Islamabad, Pakistan. E-mail: zeeshan.muhammad@iiu.edu.pk*
[b] *Department of Electrical and Computer Engineering, International Islamic University, Islamabad, Pakistan*

populated by excitons, specifically referred to as Frenkel excitons. These materials have large effective masses and low permittivity and their value for exciton binding energy at RT ranges from 40 to 700 meV.[51–54] In addition to Wannier–Mott and Frenkel excitons, a third type, known as charge transfer (CT) excitons, is worth considering. These are formed when an electron or hole is transferred across a material interface.[55,56] OILHPs, which consist of both organic and inorganic components, form a unique class of materials that combine the properties of both types. The exciton binding energy measured through experiments lies approximately between 7.4[57] and 162[58] meV for $MAPbI_3$ with different structural morphologies. Such a large difference in the measured value for the exciton binding energy, compared to the small differences in bandgap values, leads to the unexplained phenomenon of free carrier or exciton generation in the optically excited state. It remains unclear which of the two species plays an active role in optical excitation, thereby influencing the photophysical properties of the material. Many reported measurements revealed that excitons being generated at RT will dissociate spontaneously into free carriers upon photoexcitation during the duration of the sub-ps range, resulting in free carrier dominance in the subsequent optically excited processes.[59–61] Beyond the dielectric and quantum confinement effects in these materials, recent discussions on quasiparticles dressed by lattice phonons known as polarons have prompted researchers to consider their impact when studying exciton transport properties in OILHPs. Large polaron formation significantly influences the effective masses and mobility of excitons, affecting their optical transport mechanisms.[62–64] Along with the excitonic features, the formation of polarons plays a significant role in realizing the excited-state optical characteristics of OILHPs due to the existence of high exciton resonances in their transient absorption spectra and band edge absorption onsets. Therefore, despite significant progress in exciton and polaron physics in recent years, the fundamental understanding and determination of exact reliable values for exciton binding energies of OILHPs still need to be revealed.

In this article, our focus is centered on commonly studied OILHPs, thereby explaining their underlying photophysical processes and illustrating the disparities in the outcomes of various relevant experiments and theoretical approaches. This review article aims to provide an up-to-date analysis of exciton binding energy and exciton/polaron physics in OILHPs, with implications for both fundamental research and practical applications.

2. Techniques for determining exciton binding energies

Perovskite systems are commonly described using the Wannier–Mott model[65–67] due to the significantly larger effective Bohr radii of excitons compared to the lattice constant in these materials. This model relies on the assumption of effective masses of the carriers and the inclusion of the dielectric constant. Within this framework, the nth state excitonic energy can be determined by

$$E_n = E_g - \frac{R^*}{n^2} \quad (1)$$

where E_g is the bandgap energy and R^* is the effective Rydberg excitonic energy. Generally, for semiconductors, the carrier effective mass tends to be smaller as compared to that of free electrons. It is also known that the interaction between carriers is effectively screened by the lattice. This leads to the concept of the effective Rydberg energy, which can be applied to Wannier excitons by renormalizing the hydrogenic Rydberg energy (R_H = 13.6 eV) and is given by

$$R^* = E_{xb} = \frac{\mu R_H}{m_0 \varepsilon_r^2} \quad (2)$$

where $\mu = \frac{m_e m_h}{m_e + m_h}$ is the reduced exciton mass with effective masses $m_{e,h}$ for the electron and hole and ε_r is the relative dielectric constant, which describes the carrier screening by the crystal lattice. In large-bandgap materials such as LiF and Ar, Frenkel excitons are highly localized and tightly bound within a single crystal unit due to their effective Bohr radii being smaller than the lattice constant. Consequently, the Wannier–Mott model is inadequate for accurately describing Frenkel excitons. However, from the perspective of first-principles electronic structure theory, Wannier and Frenkel excitons are conceptually equivalent as they both represent excitations within a many-body system. The distinguishing feature of excitons is their collective nature, arising from superpositions of many single-particle excitations. For 3D OILHP systems, the Wannier–Mott model yields fairly accurate results, but it leads to the controversial estimation of exciton binding energy due to the large difference between static and high frequency dielectric constants (*e.g.* $\varepsilon_0 \approx$ 33–20 and $\varepsilon_\infty \approx$ 4.5–6.75 [see Table 2]). Moreover, due to the anisotropic nature of the dielectric constant (ε_∞), the calculations of exciton binding energy may be problematic as both temperature[68,69] and frequency[70,71] affect the dielectric function for OILHPs. However, for OILHPs, the static value (ε_0) may not always be a reliable estimate of the effective dielectric constant (ε_{eff}), because it is likely valid only when the exciton binding energy appears to be lower than the longitudinal optical phonon energy ($E_{LO} = \hbar\omega_{LO}$).[72]

Several experimental and theoretical approaches were deployed to reliably measure the exciton binding energies in OILHPs as shown in detail in Table 1. Experimental techniques mostly involved magneto-absorption, optical absorption, and photoluminescence (PL) spectroscopy which have both merits and demerits. Theoretical methods, such as many-body perturbation theory (MBPT) within the framework of density functional theory (DFT) and time-dependent density functional theory (TD-DFT), were also used to precisely estimate the universal values for exciton binding energies. In this section, we will discuss these techniques in detail.

2.1 Magneto-absorption studies

In magneto-absorption studies, the exciton binding energy measurement is based on the combined contributions arising from the Zeeman effect and the diamagnetic shift of excitons. In the region of a low magnetic field, when the cyclotron energy of carriers ($\hbar Be/\mu$) is significantly less than the electrostatic energy arising from interacting carriers, the excitonic energy

Table 1 Available data for measured exciton binding energy of OILHPs for different morphologies and temperatures/phases. Experimental and theoretical techniques are also mentioned for each case. The data are arranged in order from early 1994 to the latest measurements for each material

Material	Morphology/geometry	Temperature (K)/phase	Exciton binding energy (meV)	Measurement setup	Authors
$MAPbI_3$	3D	4.2	37	Magneto-absorption and Wannier–Mott model	Hirasawa *et al.*[73]
	3D	78	45	Optical absorption	Ishihara *et al.*[74]
	3D	80–300 (tetragonal)	32	Temperature dependent PL spectra (Arrhenius fitting)	Saveniji *et al.*[75]
	3D	Cubic	29	Reflectance spectra and Wannier–Mott model	Koutselas *et al.*[76]
	Thin film (<100 nm)	10–300	19 ± 3	Temperature dependent PL spectra (Arrhenius fitting)	Sun *et al.*[77]
	Thin film	4.2	50	Magneto-absorption and Wannier–Mott model	Tanaka *et al.*[78]
	Thin film (800 nm)	170–300	25 ± 3	UV-vis absorption spectra (Elliott's fitting)	Saba *et al.*[79]
	Thin film	RT	45	Optical absorption and Wannier–Mott model	Grancini *et al.*[80]
	3D bulk	RT	12.3	UV-vis absorption spectra (Elliott's fitting)	Green *et al.*[81]
	Thin film	RT	41	UV-vis absorption spectra (Elliott's fitting)	Kumar *et al.*[82]
	Thin film	13	30	Optical absorption spectra (Elliott's fitting)	Yamada *et al.*[83]
		300	6		
	Thin film (332 ± 38 nm)	RT	13	Transmission absorption spectroscopy (Elliott's fitting)	Yang *et al.*[84]
	Thin film (150 nm)	RT	7.4 ± 2	Electro-absorption (EA) spectroscopy (Elliott's fitting)	Ziffer *et al.*[57]
	3D	Cubic	12 ± 9	TD-DFT	Hakamata *et al.*[85]
	3D unit cell	Cubic	45	DFT and SOC-GW-BSE (with dielectric constant derived from SOC-DFPT)	Bokdam *et al.*[86]
	Thin film	10	13 (for defect free) 29 (for defect-bound)	Time-integrated four-wave mixing (TIFWM) spectroscopy	March *et al.*[87]
	Thin films (≈350 nm thick)	2 (orthorhombic) High temperature (tetragonal)	16 12	High field magneto-absorption and Wannier–Mott model	Galkowski *et al.*[88]
	Nanostructures	10–300	44	Temperature dependent PL spectra (Arrhenius fitting)	Zheng *et al.*[89]
	Thin film	77–340	∼43	Temperature dependent UV-vis absorption spectra	Ye *et al.*[90]
	Thin film	RT (tetragonal) 162 (orthorhombic)	19 26	Temperature dependent electro-absorption spectroscopy	Ruf *et al.*[91]
	Thin film (single crystal)	RT (tetragonal)	17	Temperature dependent photoluminescence	Shi *et al.*[92]
	Thin film	0–160 (orthorhombic)	20 ± 2	Optical absorption (Elliott's fitting)	Davies *et al.*[93]
	Quantum dots	Cubic	540	TD-DFT	Athanasios *et al.*[94]
	3D unit cell	Tetragonal	15	DFT and SOC-GW-BSE (with dielectric constant derived from SOC-DFPT)	Umari *et al.*[95]
	Thin film	200–360	11.7	Temperature and density-resolved optical spectroscopy	Liu *et al.*[96]
	Thin film ∼340–450 nm thick	10 150 >150	24 29 32	Optical absorption (Elliott's fitting) f-Sum rule	Ruf *et al.*[97]
	3D unit cells	Cubic Tetragonal Orthorhombic	58 64 66	DFT and Wannier–Mott model	Xu *et al.*[98]
	Quantum dots	250–300	162.1 ± 22.2	Temperature dependent PL spectra (Arrhenius fitting)	Parveen *et al.*[58]
	3D unit cell	Cubic	50–110 (with ε_∞ varying from 5.45 to 5.65)	DFT and Wannier–Mott model	Xu *et al.*[99]

Table 1 (*continued*)

Material	Morphology/geometry	Temperature (K)/phase	Exciton binding energy (meV)	Measurement setup	Authors
	2D mica/perovskite (6 nm) interface	RT	10	Time-resolved photoluminescence spectra	Bai *et al.*[100]
	Polycrystalline thin film	Tetragonal Orthorhombic 160–290	12.6 30 85 ± 30	Temperature dependent photoluminescence spectra Temperature dependent photoluminescence spectra	Hamada *et al.*[101]
		290 (tetragonal) 60 (orthorhombic)	11.6 24.2	Electro-absorption spectra (Elliott's fitting)	
	3D unit cell	Tetragonal	9.85	DFT and Wannier–Mott model	Ali *et al.*[102]
	Single crystal	RT	15	Modeling dispersion relations	Xiong *et al.*[103]
	3D unit cell	Cubic	43	DFT and Wannier–Mott model	Li *et al.*[104]
	Film deposited on a glass slide	300	26	UV-vis absorption spectroscopy and differential transmission (DT)	Simbula *et al.*[105]
	3D unit cell	Cubic	4.88	TD-DFT and interfragment charge transfer method (IFCT)	Gao *et al.*[106]
	Thin film	Pseudo-cubic	16.9	Edward's model and Hang-Schmitt-Rink's (HSR) model. Mott densities extracted from the carrier-density-dependent hot carrier experimental graph	Chan *et al.*[107]
	3D unit cell	Cubic	16.13	DFT and Wannier–Mott model	Basera *et al.*[108]
		—	40.6 (without polaron inclusion) 27.0 (with polaron inclusion)	Path integral molecular dynamics simulations	Park *et al.*[63]
	3D unit cell	Cubic	37	DFT and Wannier–Mott model	Biffi *et al.*[109]
	Thin film	RT	10	Optical pump THz probe	Ulatowski *et al.*[110]
$MAPbBr_3$	Single crystal 5 × 5 × 3 mm^3	4.2	76	Magneto-absorption and Wannier–Mott model	Tanaka *et al.*[78]
	Thin film	RT	37	UV-vis absorption spectra (Elliott's fitting)	Kumar *et al.*[82]
	3D bulk	RT	36.3	UV-vis absorption spectra (Elliott's fitting)	Green *et al.*[81]
	Quantum dots (average diameter of 3.3 nm)	5–300 300–400	42 375	Temperature dependent PL spectra (Arrhenius fitting)	Zhang *et al.*[111]
	Microsized bulk particles 2–8 μm	5–300	65		
	Nanoparticles	240–350	320	Temperature dependent PL spectra (Arrhenius fitting)	Zheng *et al.*[112]
	3D bulk		84		
	Thin film (86 ± 11 nm)	RT	40	Transmission absorption spectroscopy	Yang *et al.*[84]
	Single crystal (4 × 4 × 2 mm^3)	4	80–100	Temperature dependent reflectance spectra	Kunugita *et al.*[113]
	Thin films (≈350 nm thick)	2 (orthorhombic)	25	High field magneto-absorption and Wannier–Mott model	Galkowski *et al.*[88]
	3D unit cell	Cubic	71	DFT and SOC-GW-BSE	Bokdam *et al.*[86]
	Rectangular microstructures with length 1–3 μm	10–300	53.35 ± 2.60	Temperature dependent PL spectra (Arrhenius fitting)	Dai *et al.*[114]
	Single crystal (with dimensions of 3 × 3 × 3 mm)	10	15.33	Temperature dependent PL spectra	Tilchin *et al.*[115]
	Single crystal	5	20–40	Photoluminescence spectra at low temperature	Kunugita *et al.*[116]
	Single crystal	10–230	21 ± 3	Temperature dependent reflectance spectra (Lorentz model)	Thu Ha Do *et al.*[117]
	Quantum dots	Cubic	610	TD-DFT	Athanasios *et al.*[94]
	Polycrystalline film (~200 nm)	RT (tetragonal)	20	Optical absorption spectra	Shi *et al.*[92]
	2D mica/perovskite (8 nm) interface	RT	30	Time-resolved photoluminescence spectra	Bai *et al.*[100]

Table 1 (*continued*)

Material	Morphology/geometry	Temperature (K)/phase	Exciton binding energy (meV)	Measurement setup	Authors
	Thin film ∼340–450 nm thick	10	30	Optical absorption (Elliott's fitting)	Ruf *et al.*[97]
		150	38		
		>150	41	f-Sum rule	
	Thin film	280–380	25.9	Temperature and density-resolved optical spectroscopy	Liu *et al.*[96]
	Quantum dots	250–300	271.1 ± 34.1	Temperature dependent PL spectra (Arrhenius fitting)	Parveen *et al.*[58]
	Single crystal platelets (5.9–28.2 nm)	77–300	70 –150	Temperature dependent PL spectra (Arrhenius fitting)	Liu *et al.*[118]
	Single crystal	RT	15	Modeling of dispersion relations	Xiong *et al.*[103]
	Polycrystalline	RT	40	Temperature dependent PL spectra	Shi *et al.*[119]
	Thin film	RT	34.8	Optical absorption (Elliott's fitting)	Ulatowski *et al.*[120]
	3D unit cell	Cubic	27.33	DFT + Wannier–Mott model	Jain *et al.*[121]
	Film deposited on a glass slide	77–300	64	UV-vis absorption spectroscopy and differential transmission (DT)	Simbula *et al.*[105]
	3D unit cell	Cubic	5.43	TD-DFT and interfragment charge transfer method (IFCT)	Gao *et al.*[106]
	Microwires with a length of 343.5 μm	80–300	75	Temperature dependent photoluminescence spectra	Yan *et al.*[122]
	Thin film	RT (cubic)	36	Using Edward's model and Hang-Schmitt-Rink's (HSR) model. Mott densities extracted from the carrier-density-dependent hot carrier (HC) experimental graph	Chan *et al.*[107]
$FAPbI_3$	3D bulk	RT	8.4	UV-vis absorption spectra (Elliott's fitting)	Green *et al.*[81]
	Thin films (≈350 nm thick)	2 (orthorhombic)	14	High field magneto-absorption and Wannier–Mott model	Galkowski *et al.*[88]
		High temperature (tetragonal)	10		
	3D unit cell	Cubic	35	DFT and SOC-GW-BSE	Bokdam *et al.*[86]
	Thin film	150–295 (α-phase)	8.1	Temperature dependent PL spectra (Arrhenius fitting)	Fang *et al.*[123]
		5–110 (β-Phase)	18		
	Thin film	80–340	29	Temperature dependent PL spectra	Yuan *et al.*[124]
	Single crystal	α-Phase (trigonal)	43.5	UV-vis absorption spectra	Sachenko *et al.*[125]
	Nanostructures	10–300	8.4	Temperature dependent PL spectra (Arrhenius fitting)	Zheng *et al.*[89]
	Thin single crystal nanoplates	RT	∼10	Time-resolved photoluminescence (TRPL)	Fu *et al.*[126]
	3D unit cell	Tetragonal	17	SR-DFT and SOC-GW	Umari *et al.*[95]
	Thin film	10	5.3	THz photoconductivity spectra	Davies *et al.*[127]
	3D unit cell	Cubic	50–85 (with ε_∞ varying from 5.45 to 5.65)	DFT and Wannier–Mott model	Xu *et al.*[99]
	Thin film	200–360	9.95	Temperature and density-resolved optical spectroscopy	Liu *et al.*[96]
	Single crystal	20–240	∼2–5	Temperature dependent absorption spectra (Elliott's fitting)	Johnston *et al.*[128]
	3D unit cell	Cubic	13.30	DFT and Wannier–Mott model	Basera *et al.*[108]
	3D unit cell	Cubic	4.93	TD-DFT and interfragment charge transfer method (IFCT)	Gao *et al.*[106]
	3D bulk	Tetragonal	93	DFT and SOC-GW-BSE (with dielectric constant derived from SOC-GW)	Muhammad *et al.*[129]
		Hexagonal	567		
	Thin film (with a thickness of 400 nm)	RT	11	Optical absorption (Elliott's fitting)	Jeon *et al.*[130]

Table 1 (*continued*)

Material	Morphology/geometry	Temperature (K)/phase	Exciton binding energy (meV)	Measurement setup	Authors
	Quantum dots	80–390	69.2	Temperature dependent PL spectra (Arrhenius fitting)	Wang *et al.*[131]
	Bulk		91		
	Thin film	0–300	20–3	Optical absorption (Elliott's fitting)	Elmestekawy *et al.*[132]
$FAPbBr_3$	3D bulk	RT	31.8	UV-vis absorption spectra (Elliott's fitting)	Green *et al.*[81]
	Thin films (≈350 nm thick)	2 (orthorhombic)	22	High field magneto-absorption and Wannier–Mott model	Galkowski *et al.*[88]
		High temperature (tetragonal)	24		
	3D unit cell	Cubic	60	DFT and SOC-GW-BSE	Bokdam *et al.*[86]
	Rectangular microstructures with length 1–3 μm	10–300	21.67 ± 1.62	Temperature dependent PL spectra (Arrhenius fitting)	Dai *et al.*[114]
	Nanocrystals (12–14 nm)	180–360	170	Time-resolved PL spectra (Arrhenius fitting)	Perumal *et al.*[133]
	Nanocrystals	90–350	160	Time-resolved PL spectra (Arrhenius fitting)	Yang *et al.*[134]
	Nanocrystals (5–20 nm)	0–300	∼57.5	Time-resolved PL spectra (Arrhenius fitting)	Han *et al.*[135]
	2D nanoplatelet thin films	120–300	287.5	Temperature dependent PL spectra	Fang *et al.*[136]
	Nanocrystals	100–380	∼68.4	Temperature dependent PL spectra (Arrhenius fitting)	Liu *et al.*[137]
	Thin film	280–380	9.95	Temperature and density-resolved optical spectroscopy	Liu *et al.*[96]
	Quasi-2D co-interlayer	78–290	228	Temperature dependent PL spectra	Meng *et al.*[138]
	Nanocrystals encapsulated by siliceous nanosphere	RT	5	Optical absorption spectra	Sui *et al.*[139]
	Nanocrystals with an average length of ∼12 nm	4	∼17	Temperature dependent PL spectra	Liu *et al.*[140]
	Nanoplatelets (n = 2)	RT	112	Temperature dependent PL spectra (Arrhenius fitting)	Peng *et al.*[141]
	Nanocrystals (6–8 nm)	80–175	42.3	Temperature dependent steady state PL spectra (Arrhenius fitting)	Wang *et al.*[142]
		175–400	80.2		
	Square and quasi-circular microdisks having typical edge lengths/diameters ranging from a few to tens of micrometers with thicknesses ranging from 200 nm to a few micrometers	75–300	24.6	Temperature dependent PL spectra	Li *et al.*[143]
	Nanocrystals	80–300	51	Temperature dependent PL spectra (Arrhenius fitting)	Zhang *et al.*[144]
	3D unit cell	Cubic	22.06	DFT + Wannier–Mott model	Jain *et al.*[121]
	Thin film	Cubic	9.3	Edward's model and Hang-Schmitt-Rink's (HSR) model. Mott densities extracted from the carrier-density-dependent hot carrier experimental graph	Chan *et al.*[107]
	3D unit cell	Cubic	5.29	TD-DFT and interfragment charge transfer method (IFCT)	Gao *et al.*[106]
	Thin film with 350 nm thickness	Cubic	53	Optical absorption (Elliott's fitting)	Qaid *et al.*[145]
	Nanocrystals	—	69.668	Temperature dependent PL spectra	Zhang *et al.*[146]
$MAPbBr_{3-x}Cl_x$ $(0 \leq x \leq 3)$	Thin films	Cubic	21 ± 1–52 ± 6	Optical absorption spectra	Comin *et al.*[147]
$MAPbI_{3-x}Cl_x$	Polycrystalline film	150–290	55 ± 21	Temperature dependent PL spectra	D'Innocenzo *et al.*[148]
$FA_{0.81}MA_{0.15}Pb(I_{0.83}6Br_{0.15})_3$	Thin film	77–340	∼13	Temperature dependent UV-vis absorption spectra	Ye *et al.*[90]
$Cs_x(FA_{0.4}MA_{0.6})_{1-x}PbI_{2.8}Br_{0.2}$ $(0 \leq x \leq 0.2)$	Film	303.15–833.15	8.0–10.1	UV-vis absorption spectra (Elliott's fitting)	Liu *et al.*[149]

Table 1 (*continued*)

Material	Morphology/geometry	Temperature (K)/phase	Exciton binding energy (meV)	Measurement setup	Authors
$FA_xMA_{1-x}PbI_3$ ($0.2 \leq x \leq 0.8$)	Nanostructures	10–300	20.8 ± 3.9–28 ± 3.9	Temperature dependent PL spectra (Arrhenius fitting)	Zheng *et al.*[89]
$MAPbI_{3-x}Br_x$ ($0 \leq x \leq 3$)	Nanocrystalline solid films	RT	9–15	Electro-absorption spectra	Awasthi *et al.*[150]
$FA_{0.85}Cs_{0.15}PbI_{2.9}Br_{0.1}$	Thin film	77–250	5.9 ± 2.0	Temperature dependent spectroscopic ellipsometry	Whitcher *et al.*[151]
$(MA_{0.13}FA_{0.87})PbI_3$	Single crystal	400	40	Optical absorption spectra (Elliott's fitting)	Chen *et al.*[152]
		4.4	16		
$FAPbBr_{3-x}Cl_x$	Nanocrystals	75–270	137 (for Br-ligand)	Temperature dependent PL spectra (Arrhenius fitting)	Zhang *et al.*[153]
Br-ligand → 14.6 nm					
Br-ligand → 12.1 nm			223 (for Cl-ligand)		
$MAPbBr_{3-x}Cl_x$ ($0 \leq x \leq$ 25 mol%)	3D bulk ($2 \times 2 \times 1$ supercell)	Cubic	67–66	DFT and Wannier–Mott model	Rybin *et al.*[154]
$FAPb(I_{1-x}Br_x)_3$ ($0 \leq x \leq 1$)	3D bulk ($1 \times 1 \times 2$ supercell)	Cubic	74–112	DFT and SOC-GW-BSE	Muhammad *et al.*[155]
$Cs_xFA_{1-x}PbI_3$ ($0.25 \leq x \leq$ 0.75)	Quantum dots	80–390	53.1–36.4	Temperature dependent PL spectra	Wang *et al.*[131]
$FA_{0.85}Cs_{0.15}Pb(I_{0.97}Br_{0.03})_3$	Thin film	RT	38 ± 4	Steady-state and transient absorption spectra (Elliott's fitting)	Bao *et al.*[64]

shift becomes[156]

$$E(B) - E_0 = \pm\frac{1}{2}\mu_B g B + c_0 B^2 \quad (3)$$

Here E_0 represents the exciton ground state energy, μ_B is the Bohr magneton, g is the Landé g-factor, and c_0 is the diamagnetic coefficient that can be expressed as

$$c_0 = \frac{1}{\mu^3}\left(\frac{2\pi\varepsilon_0\varepsilon_r\hbar^2}{e}\right)^2 \quad (4)$$

The value of c_0 is helpful in determining the exciton radius r_E and reduced mass μ provided that the relative dielectric constant ε_r is known[78]

$$\frac{r_E}{r_H} = \left(\frac{\varepsilon_r c_0}{c_H}\right)^{\frac{1}{3}} \quad (5)$$

$$\frac{\mu}{m_0} = \left(\frac{\varepsilon_r^2 c_H}{c_0}\right)^{\frac{1}{3}} \quad (6)$$

$$\frac{E_{xb}}{E_H} = \left(\frac{c_H}{\varepsilon_r^4 c_0}\right)^{\frac{1}{3}} \quad (7)$$

where r_H, c_H, m_0, and E_H are the hydrogen atom (Bohr) radius, diamagnetic coefficient, the rest mass of the electron, and binding energy.

The magneto-absorption method was first adopted to determine the exciton binding energy for $MAPbI_3$ microcrystals at low temperatures. The magneto-absorption spectra of $MAPbI_3$ using a magnetic field of ~40 T at a lower temperature (4.2 K) were investigated by Hirasawa *et al.*[73] They first measured the value for c_0 which is 2.7 μeV T^{-2}. Next, they found an E_{xb} of 37 meV with r_B = 28 Å and μ = 0.12 using ε_∞ = 6.5. Later Tanaka and coworkers[78] used the same procedure of Hirasawa with magnetic field B = 50 T which yielded a smaller value of c_0 which is 1.35 μeV T^{-2} for $MAPbI_3$ and 1.28 μeV T^{-2} for $MAPbBr_3$. Opting the value of ε_∞ calculated by Hirasawa *et al.*, an E_{xb} of 50 meV with r_B = 22 Å and μ = 0.15 and similarly an E_{xb} of 76 meV with r_B = 20 Å and μ = 0.13 were obtained for $MAPbI_3$ and $MAPbBr_3$ thin films, respectively.

In comparison to other methods, analyzing the shift in high field excitonic absorption is quite simple, that is, the considerably widened excitonic transition shift can be monitored easily thereby improving the accuracy of data analysis. However, there are three main issues with the early studies on perovskites in magnetic fields. The first is the arbitrary selection of the dielectric constant and the second is considering the field strength of 50 T as the minimum field limit. According to Lin *et al.*, there is some controversy about whether ε_∞ should be included in the measurement of E_{xb}.[70] An exciton binding energy E_{xb} = 1.7–2.1 meV may be obtained by analyzing Tanaka *et al.*'s data using the static dielectric constant of 70.[70] Finally, the third issue is that the measurements were based on the exciton diamagnetic coefficient in MA spectra and thus the calculated exciton binding energy was purely based on

approximating the hydrogenic (Wannier–Mott) model which may not be valid or least valid for OILHPs.

Recently, with advanced techniques, a much stronger magnetic field of more than 200 T can be used to study both exciton absorption (1s and 2s) and the intraband free carrier absorption[84,88,157–159] as shown in Fig. 1(a)–(d) for $MAPbI_{3-x}Cl_x$ and $FAPbI_3$. With extreme magnetic fields, band-to-band multiple transitions of free carriers are observed at higher energies larger than the free exciton transition energies. Such transitions are observed between van Hove singularities of the Landau states with energies described by

$$E_N = E_g + \left(N + \frac{1}{2}\right)E_\omega \pm \frac{1}{2}g_{eff}\,\mu_B B \tag{8}$$

where $N = 1, 2, 3\ldots$ and so on is the orbital quantum number of the Landau state, $E_\omega = \hbar\omega_c$ is the exciton cyclotron energy, and g_{eff} is the effective g-factor. The energy fluctuation of the Landau states as a function of the magnetic field imposes a substantial limit on the bandgap energy and exciton's reduced mass. Makado and McGill[160] developed a numerical model that was used to investigate the exciton diamagnetic shift in the hydrogen atom in the presence of a magnetic field. This model can be used across all magnetic field strengths. It solely relies on the exciton reduced mass and exciton binding energy as input data, making it unnecessary to assume a specific value for the dielectric constant prior. Due to the high field measurements, two of the three limitations that were included in the earlier magneto-absorption investigations are no longer valid. Fig. 1(e) and (f) shows the field-dependent 1s and 2s excitonic states along with Landau energy states that are concurrently plotted on the fan chart layout. The reduced mass is unaffected by free carrier transitions, leaving the exciton binding energy as the sole parameter in the simulated hydrogen model. This enables the accurate and consistent measurement of the exciton binding energy, bandgap, reduced exciton mass, and effective dielectric while keeping carriers' effective mass constant.

Using the high field magneto-absorption, Galkowski *et al.*[88] estimated E_{xb} of 14 meV and 16 meV at 2 K and μ of 0.09 and 0.104 for $FAPbI_3$ and $MAPbI_3$ respectively. Similarly, at 161 K, they also found E_{xb} of 10 meV and 12 meV for $FAPbI_3$ and $MAPbI_3$ respectively. In this scenario, the 1s–2s splitting (Δ_{1-2}) in the hydrogen model can be deployed to directly determine E_{xb}. Although thin films have a lower E_{xb}, their transition strength is significantly higher compared to that observed in single crystals. Remarkably, the effective mass and E_{xb} derived from magneto-optical thin film experiments differ from those obtained from single crystals. This finding shows that some features of the excitonic behavior are not fully interpreted from the data of high-field magneto-optical experiments. Notably, the shift in band dispersion to non-parabolic cannot account for the observed decrease in reduced mass at elevated fields. The magneto-optical studies still describe accurately the excitonic transitions and upper bound exciton binding energy. However, they fail to explain band-to-band excitonic absorption at room or higher temperatures. Meanwhile, the decrease in E_{xb} observed in magneto-optical studies at temperatures slightly above the phase transition, along with data from electroabsorption[57,150] and other absorption studies,[83,161] strongly supports the hypothesis that E_{xb} is reduced at RT by a few meV.

2.2 Absorption studies

The absorption methods are probably the most classical approach for estimating E_{xb} in semiconductors having direct bandgap. For high quality samples, the measurement of the energy gap between the Wannier type excitonic energy levels, which can be seen individually as peaks in the absorption spectrum at the band edge, can be described through Elliott's equation.[162]

$$\alpha(\hbar\omega) = \Gamma_{cv}\left[\xi(\hbar\omega - E_g)\cdot\frac{\pi e^{\pi x}}{\sinh(\pi x)} + E_{xb}\sum_{i=1}^{\infty}\frac{4\pi}{n^3}\cdot\delta\left(\hbar\omega - E_g + \frac{E_{xb}}{n^2}\right)\right] \tag{9}$$

where the frequency dependent Γ_{cv} represents the proportionality constant that considers the intraband electric dipole transition matrix element. ξ is the Heaviside step function, δ represents the delta function, and $x = \sqrt{E_{xb}(\hbar\omega - E_g)}$. In this model the first part represents a comprehensive intrinsic absorption continuum state in the presence of Coulomb interactions. Within this framework, the photon-to-exciton conversion rate completely determines the energy dissipation rate from the photon field, thereby establishing a direct link between the two processes.[162,163] Such correlation will increase the absorption relative to vanishing excitonic effects which is often referred to as Sommerfeld amplification. The latter term describes the series of optically allowed excitonic transitions near the bandedge with discrete energy levels as in the hydrogen atom. Fig. 2(a) shows a typical absorption spectrum near the bandedge produced by arbitrary line broadening and changing the constants in eqn (9). The first three exciton peaks (designated as 1S, 2S, and 3S) in this hypothetical scenario are resolved below the continuum state. However, with increasing n the amplitude of the excitonic peaks diminishes, and the spectra across a small energy range approach a constant thereby merging into the continuum at the bandedge. The density of states close to the bandgap would vanish when no excitonic effects are considered [red curve, Fig. 2(a)].

For example, Ruf *et al.*[97] obtained Elliott fitted spectra (red curve) comprised of continuum states (green curve) due to free carrier resonances and discrete excitonic peaks (blue curve) at 20 K for $MAPbBr_3$ and Cs-containing mixed perovskites $Cs_{0.10}[(FAMA)Pb(IBr)_3]$ (designated as Cs0.10) and $Cs_{0.05}[FAMAPb(IBr)_3]$ (designated as Cs0.05) as depicted in Fig. 2(b)–(d) respectively. These spectra clearly illustrate that Elliott fitting purely relies on the relevant bandgap energy E_g and exciton binding energy E_{xb} as outlined in the summary provided in Fig. 2(f). Since the excitonic peak energy is lower than E_g by the magnitude of E_{xb}, a thorough understanding of E_{xb} is crucial for accurate measuring E_g as excitonic effects play a vital role in analyzing absorption spectra at RT. With increasing temperature,

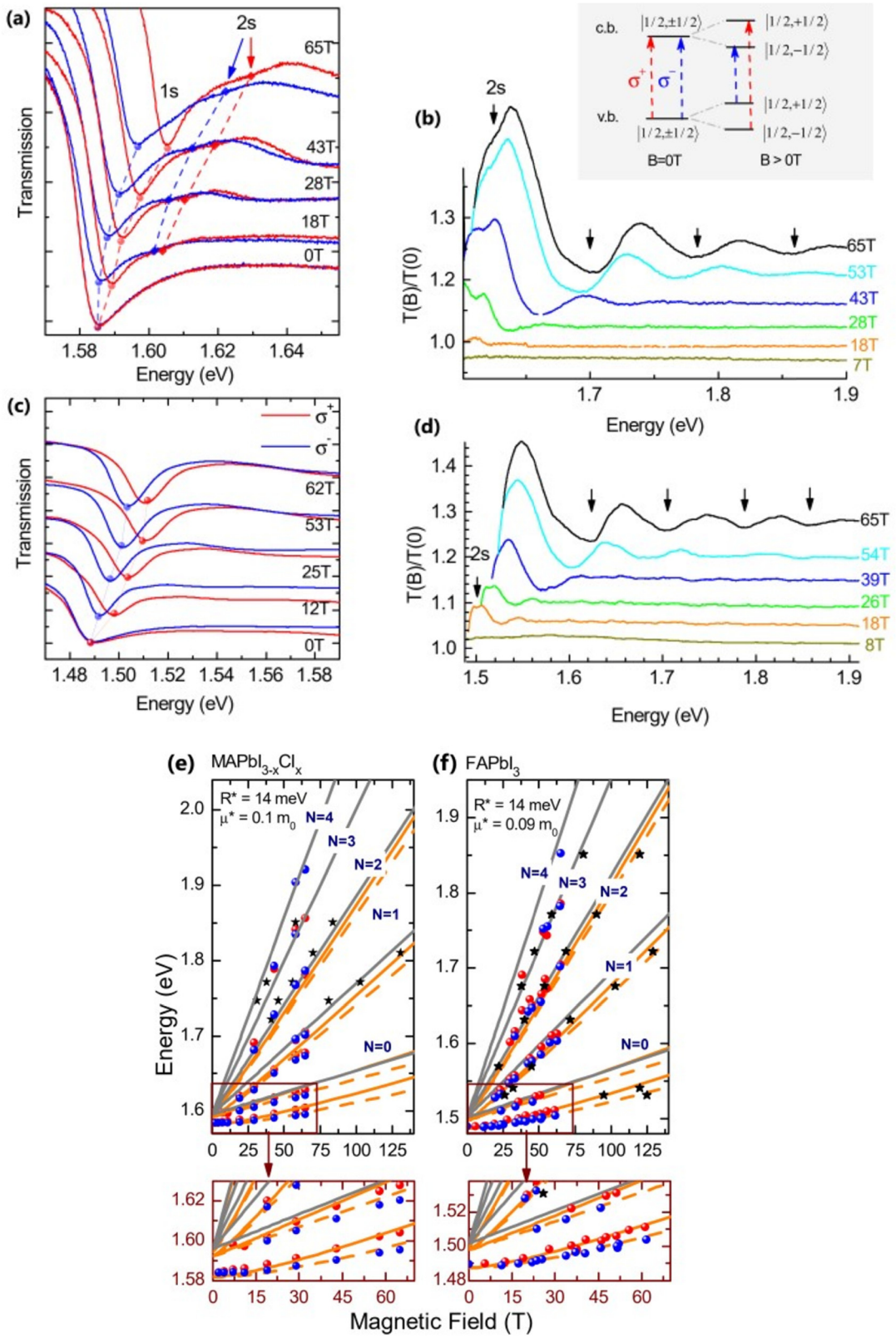

Fig. 1 (a)–(d) Transmission data at low temperatures for $MAPb_{3-x}Cl_x$ and $FAPbI_3$ respectively. The red and blue lines in panels (a) and (c) show σ^+ and σ^- polarized light, respectively. The inset displays the selection criteria for each of the two polarizations. The data collected at various magnetic field strengths are represented by different colors in panels (b) and (d). (e) and (f) The transition energies for $MAPbI_{3-x}Cl_x$ and $FAPbI_3$ respectively derived from the experimental data and the results of the fit. The orange and gray lines indicate the fitting data of theoretical results. The interband transitions between Landau states are shown by grey lines. The strongly bound levels of the hydrogen-like exciton are depicted by the orange lines. The solid and dashed lines in (e) and (f) indicate the Zeeman split transitions. Here R^* denotes exciton binding energy. The low field and low energy portion of the whole fan chart diagram is magnified below each graph. Reprinted with permission,[88] Copyright 2019, Royal Society of Chemistry.

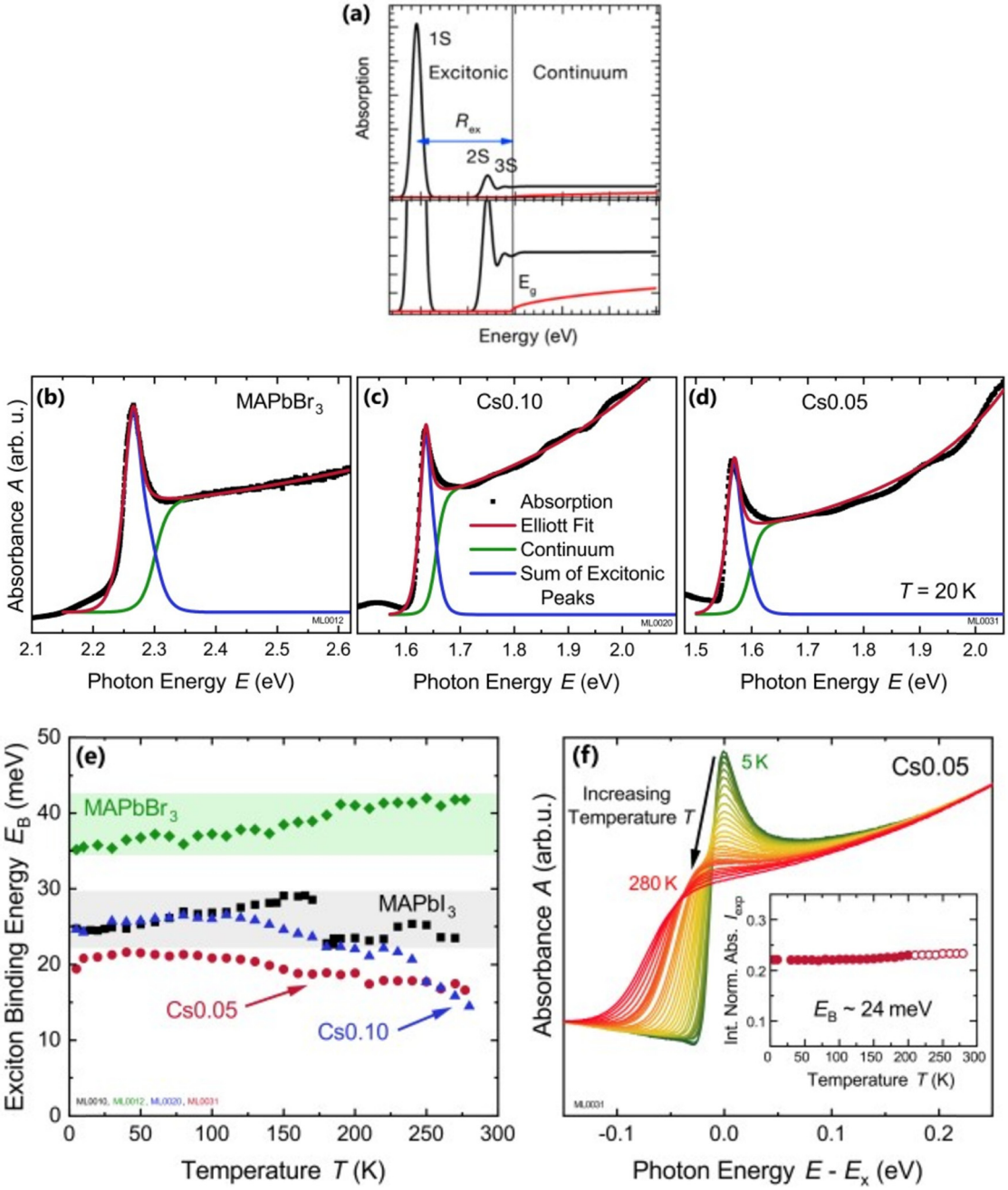

Fig. 2 (a) An example of bandedge absorption spectrum based on eqn (9). The lowest first, second, and third exciton states are approximated with arbitrary broadening which saturates into the continuum near the bandedge. The exciton binding energy is the difference in energy between the free carrier absorption edge and the first exciton peak. The red curve represents the absorption spectrum of free carriers while neglecting the excitonic effects. A magnified image is shown below the main graph. Reprinted with permission,[164] Copyright 2018, American Chemical Society. (b)–(d) Absorption spectra at 20 K as a function of photon energy for $MAPbBr_3$, $Cs_{0.01}FA_{0.765}MA_{0.135}Pb(I_{0.765}Br_{0.235})_3$ (depicted as Cs0.10), and $Cs_{0.05}(FA_{0.83}MA_{0.17})_{0.95}$-$Pb(I_{0.83}Br_{0.17})_3$ (depicted as Cs0.05) respectively. The red line represents Elliot's fit while the green and blue lines correspond to excitons and continuum contribution. (e) Estimation of exciton binding energy E_{xb} for $MAPbI_3$, $MAPbBr_3$, Cs0.01, and Cs0.05 according to the absorption spectra of (b, c, d). (f) Normalized spectra for Cs0.05 from 5 K to 280 K with respect to energy shift by excitonic peak E_x whereas the inset represents the integrated normalized spectra I_{exp}. Adapted from ref. 97, Copyright 2019, American Institute of Physics.

the discrete excitonic feature is difficult to distinguish due to the significant increase in excitonic absorption broadening as shown in Fig. 2(e) for Cs0.05. In such circumstances, E_{xb} cannot reliably be measured. Logically, this is true for E_g, although it is considerably less significant as $E_g \gg E_{xb}$. The inverse correlation between excitonic absorption broadening and E_{xb} affects the prominent position of the excitonic peak in the spectrum which can become more challenging for compounds with lower E_{xb}. Consequently, the absorption spectra are usually unclear with some parameters that approximate transition broadening to evaluate E_{xb} through

the Elliott formula.[83,161,165] The band nonparabolic behavior is also frequently taken into consideration to match the results with the experimental data.[97,147] However, with a high uncertainty in the extracted E_{xb}, such observations lead to doubtful results due to the involvement of a large number of fitting parameters. The same scenario can be noticed from large variations in the measured value of E_{xb} using this method for OILHPs (Table 1). Furthermore, there is disagreement about the temperature dependence of E_{xb}. Some studies show a constant E_{xb}[79,97,165] in the temperature range 10–300 K, whereas others report strong evidence of temperature-dependent E_{xb}.[83,166] These conflicting findings raise serious concerns about the scientific reliability of the E_{xb} derived from the Elliott theory. For example, Saba *et al.* extracted an identical E_{xb} of 25 meV for two different temperatures 300 and 170 K, by using the absorption onsets for $MAPbI_3$.[79] Kumar *et al.* obtained an E_{xb} of 41 meV for $MAPbI_3$ at RT.[82] According to Even *et al.*, the E_{xb} of $MAPbI_3$ increases sharply to 15 meV in the low temperature 0–160 K range (orthorhombic phase) but remains relatively constant at 5 meV in the high temperature 160–330 K range (tetragonal phase).[166] Yamada *et al.* showed that when the temperature drops from 300 to 13 K, E_{xb} gradually increases from 6 meV up to 30 meV.[83] In an attempt to eliminate the temperature dependence issue, Sestu *et al.* applied an alternative method called the f-sum rule, which normalizes the variation in integrated absorption due to temperature to a certain energy. This enables for the explicit determination of the independent influence of linewidth broadening and E_{xb} on the shape of the absorption line.[165] Using this method, the authors deduced an E_{xb} of 29 meV for $MAPbBr_3$ which is nearly independent of temperature across the range of 80–300 K. However, for $MAPbI_3$ an E_{xb} of 34 meV in the low temperature range (80–140 K) and 29 meV in the high temperature range (170–300 K) was obtained.

Alternatively, E_{xb} can be deduced by analyzing the full width at half maximum (FWHM) of the temperature-dependent excitonic absorption.[148] The broadening of the excitonic transition can be described as

$$\Delta\Omega = \Delta\Omega_0 + \Delta\Omega_\tau e^{-\frac{E_{xb}}{k_B T}} \quad (10)$$

where $\Delta\Omega_0$ denotes the broadening parameter independent of temperature and the term $\Delta\Omega_\tau \exp(-E_{xb}/k_B T)$ represents the thermally dissociated exciton broadening. Using this approach for $MAPbI_{3-x}Cl_x$, E_{xb} was found to be 55 ± 10 meV. Due to the band-to-band absorption and the overlap of excitons, accurate experimental determination of the FWHM might pose challenges.

2.3 Temperature-dependent photoluminescence studies

Temperature-dependent photoluminescence (PL) is another technique that experimentally determines E_{xb} which is based on fitting of integrated PL intensity $I(T)$ as a function of temperature using the Arrhenius formula,

$$I(T) = \frac{I_0}{A \exp\left(-\frac{E_{xb}}{k_B T}\right) + 1} \quad (11)$$

In general, the PL intensity diminishes with increasing temperature, which is associated with thermally induced exciton dissociation, and the process is usually known as PL quenching.[75] Fig. 3(a) and (b) demonstrate an example of extracting E_{xb} from the temperature-dependent PL spectra analysis.[137] However, using this method a large variation in the values of E_{xb} was observed. For instance, E_{xb} = 10 meV (RT)[110] and 162 meV (250–300 K)[58] for $MAPbI_3$, 42 meV (5–300 K)[111] and 320 meV (240–360 K)[112] for $MAPbBr_3$, 8.1 meV (150–295 K)[123] and 91 meV (80–390 K)[131] for $FAPbI_3$, and 22 meV (10–300 K)[114] and 170 meV (180–360 K)[133] for $FAPbBr_3$. Significantly, these values are much larger than those reported in absorption studies. It is perhaps insufficient to attribute thermal quenching solely to thermally induced exciton dissociation. Furthermore, the origin of large deviations in E_{xb} evaluated by this technique may be partially attributed to shallow trap states and the complex time dependence of the radiative recombination rate in OILHP.[46,167,168]

2.4 Theoretical methods

Different theoretical techniques have been implemented to extract the exciton binding energy for OILHPs. Such approaches that are based on density functional theory (DFT) and the hydrogenic model have nevertheless yielded much higher

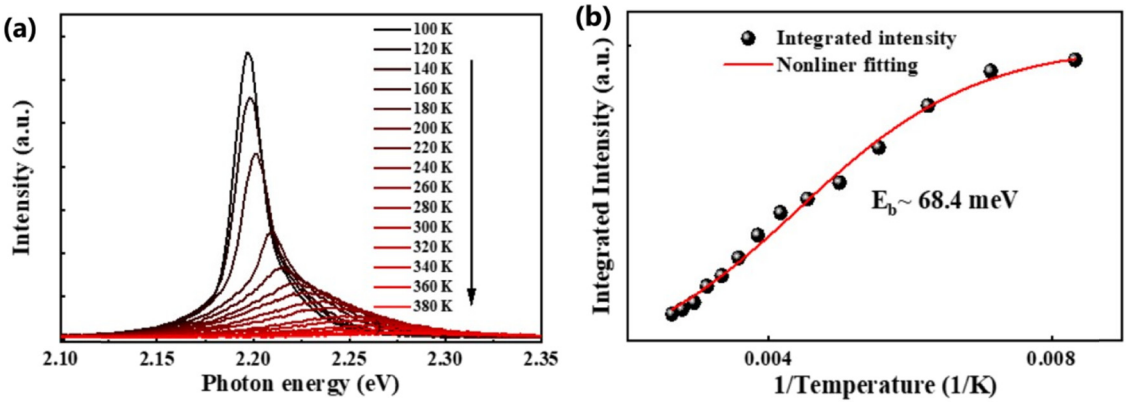

Fig. 3 (a) Temperature-dependent PL spectra of the $FAPbBr_3$ NCs from 100 K to 380 K. (b) The integrated PL intensity with respect to temperature; the red line corresponds to nonlinear fitting. Adapted from ref. 137, Copyright 2019, American Chemical Society.

values for E_{xb} as compared to experiments (Table 1). Some of the commonly used techniques are described in the following.

2.4.1 Many body perturbation theory method. The many body perturbation theory (MBPT)[169] method derived from first principles is a useful tool to accurately describe the quasiparticle excitations and excitonic features in materials. It is based on electronic self-energy, which incorporates many-body exchange and correlation effects in addition to the Hartree potential. Such a framework allows for consideration of quasiparticles, which behave like single particles due to the coulombic screening. Adopting the MBPT approach, the exciton binding energies are estimated using the GW-BSE (Green's function and Bethe–Salpeter equation) method, which considers electron–hole (e–h) and electron–electron (e–e) interactions beyond the ground state of DFT. Fig. 4 depicts the schematic performances of DFT, GW, and GW-BSE approaches for bandgap energy E_g calculations. The GW approach enhances DFT-bandgap, whereas GW-BSE accounts for excitonic effects in optical spectra, allowing the optical bandgap and thus exciton binding energy to be determined. The screening and excitonic

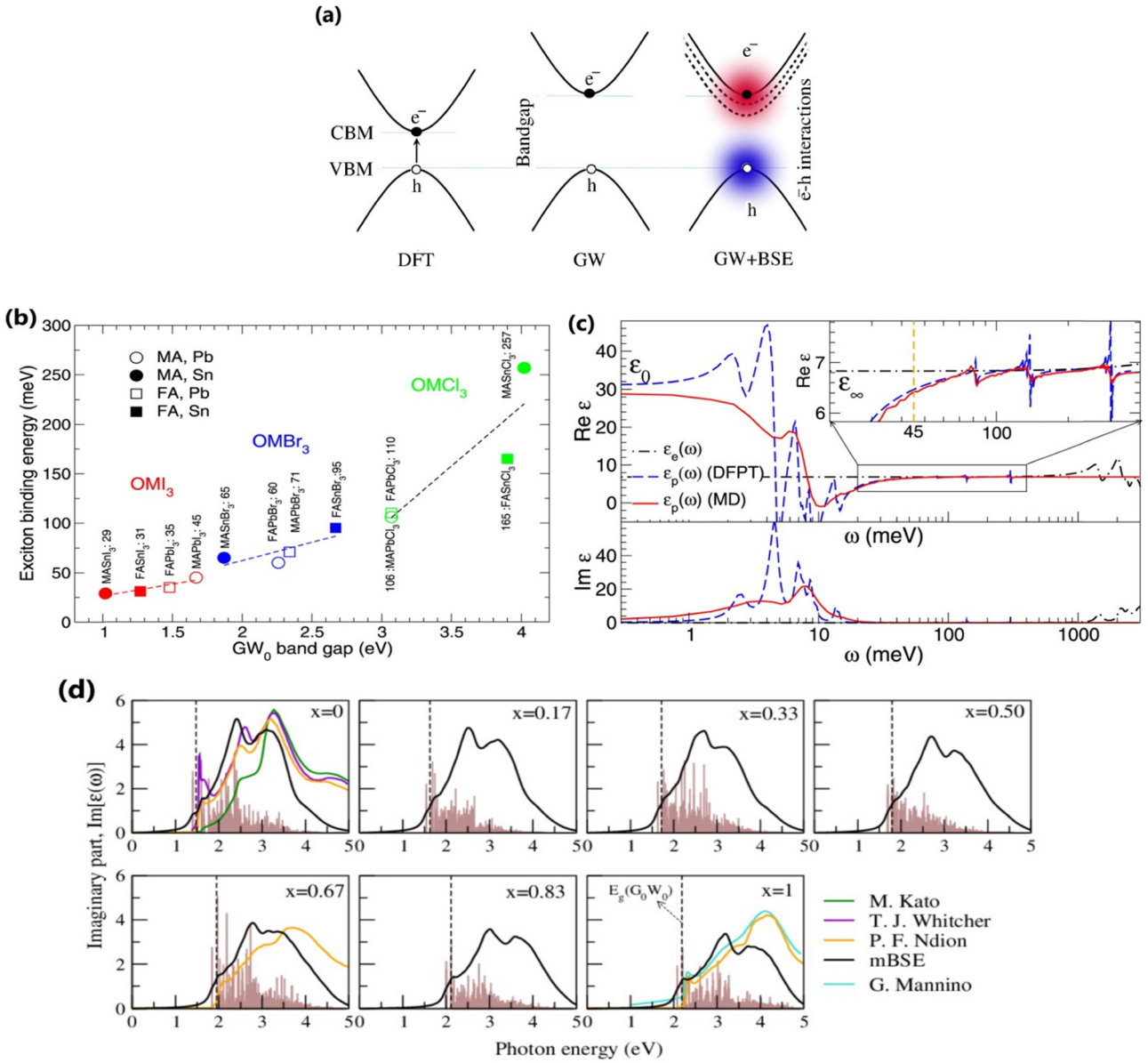

Fig. 4 (a) Schematic representations of DFT, GW, and GW+BSE approaches for bandgap E_g calculations. (b) Electronic [$\varepsilon_e(\omega)$] and ionic [$\varepsilon_p(\omega)$] contribution to the dielectric function of $MAPbI_3$. The dashed blue and solid red lines correspond to the data collected from the MD (T = 300 K) and DFPT (T = 0 K) methods respectively. The inset shows an enlarged image of Re[$\varepsilon_p(\omega)$] near E_{xb} = 45 meV. (c) Calculated E_{xb} with respect to GW bandgaps for various OILHPs using the DFT based mBSE method. Adapted from ref. 86, Copyright 2016, Springer Nature. (d) Calculated excitonic imaginary part of the dielectric function for the $FAPb(I_{1-x}Br_x)_3$ alloy along with comparison to different experimental data.[151,178–180] The dashed line indicates the corresponding GW bandgap. The brown histogram represents the calculated optical transition oscillator strengths. Reprinted with permission,[155] Copyright 2020, Springer Royal Society of Chemistry.

properties can be determined by solving BSE incorporating the quasi-particle energies (E^{QP}) from GW calculations as described by ref. 170–173

$$\left(E_{ck}^{QP}-E_{vk}^{QP}\right)\Psi_{cvk}^{J}+\sum_{c'v'k'}\left\langle cvk\middle|K^{eh}\middle|c'v'k'\right\rangle\Psi_{c'v'k'}^{J}=\Theta^{J}\Psi_{cvk}^{J} \quad (12)$$

where Ψ_{cvk}^{J} is the Jth order exciton wave function, K^{eh} is the interacting e–h kernel and Θ^{J} corresponds to excitation energies of the Jth state. The subscripts c, v, and k represent indices for conduction bands, valence bands, and k-points. Since the GW-BSE approach involves a large number of basis sets, achieving well-converged optical spectra and exciton binding energies at higher k-mesh values is challenging due to the high computational cost. Therefore, an alternative approach termed model BSE (mBSE) suggested by Liu *et al.*[174] can be adopted in which the GW based dielectric function is approximated within the diagonal matrix using an analytical model dielectric function for the diagonal elements.

$$\varepsilon^{-1}(|\mathbf{W}|) = 1 - (1 - \varepsilon_{\infty}{}^{-1})\exp(-|\mathbf{W}|^2/4x_r{}^2) \quad (13)$$

where ε_{∞}, x_r, and $|\mathbf{W}|$ are the ion-clamped or high-frequency dielectric constant, range-separation parameter, and plane-wave vector, respectively. Such method directly interprets the optical spectra and exciton binding energies for OILHPs from first-principles. Using the GW and mBSE approach, Bokdam *et al.*[86] calculated the exciton binding energy as the difference of fundamental bandgap E_g and optical bandgap E_{opt} for various organic–inorganic metal halide perovskites with lattice vibrations fixed. The calculated E_{xb} ranges from 29 meV to 257 meV with an increasing GW bandgap following the halogen's ionic size reduction from I → Br → Cl as shown in Fig. 4(b). However, they elaborated that ionic screening that influences the exciton binding energy is almost temperature independent but causes a substantial increase in static dielectric constant ε_0 using the density functional perturbation theory (DFPT)[175–177] method compared to molecular dynamics (MD) calculations as shown in Fig. 4(c). They further stated that the formation of polarons (as discussed in Section 4) is responsible for lowering the fundamental bandgap in halide perovskites at RT upon optical excitation. Similarly, Muhammad *et al.*[155] measured E_{xb} for various compositions of the $FAPb(I_{1-x}Br_x)_3$ alloy. They showed that E_{xb} increases (from 74 meV to 112 meV) with increasing Br content, which also follows the increasing trend in bandgap energy. From their GW-BSE based optical analysis, they found that the calculated excitonic spectra align well with the experimental data and an overall blue shift is observed with increasing Br concentration as shown in Fig. 4(d). Such optical behavior as well as the increase in exciton binding energy was attributed to a decrease in transition oscillator strengths near the first peak of the corresponding spectra and a decrease in high frequency dielectric constant ε_{∞}. In another study, the same authors also evaluated E_{xb} for temperature-dependent different phases of $FAPbI_3$.[129] They showed that E_{xb} is much higher in the low-temperature hexagonal phase (567 meV) as compared to the high-temperature cubic (74 meV) and tetragonal (93 meV) phases of $FAPbI_3$. These findings suggest a clear relationship between the dynamics of the PbI_3 sublattice and the rotational entropy of the FA molecule that is closely correlated with variations in E_{xb}. The GW and mBSE methods can generate excitonic optical spectra and converged values for E_{xb}; however, they require heavier k-meshing, resulting in significant computational cost.

To deal with the experimental overestimation in E_{xb}, Umari *et al.*[95] introduced the frequency dependent effective dielectric constant $\varepsilon_{eff}{}^{-1}$ in which the dielectric function $\varepsilon(\omega)$ includes phonon induced screening that can be formulated as

$$\varepsilon_{eff}{}^{-1} = 1 + \frac{2}{\pi}\int_0^{\infty}\frac{\mathrm{Im}\left[\varepsilon^{-1}(\omega)\right]}{E_{xb}+\omega} \quad (14)$$

where $\mathrm{Im}[\varepsilon^{-1}(\omega)]$ represents the usual energy loss function which can be obtained within the framework of DFPT. Now clearly ε_{eff} is E_{xb} dependent; therefore the function $\varepsilon_{eff}(E_{xb})$ can be defined effectively by using eqn (14), which accounts for frequency integration. Replacing $\varepsilon_{\infty}{}^{-1}$ by $\varepsilon_{eff}{}^{-1}$ in eqn (13), the condition for self-consistent fully relativistic BSE based E_{xb} can be described as

$$\widetilde{E_{xb}} = E_{xb}\left[\varepsilon_{eff}\left(\widetilde{E_{xb}}\right)\right] \quad (15)$$

Using this approximation with ε_{eff} = 12 (ε_{eff} = 9.5), an E_{xb} of 15 meV (19 meV) is obtained for $MAPbI_3$ derived from SOC-DFT (scalar relativistic DFT) calculations. The authors also inferred that exciton screening is not caused by the rotational dynamics or by its steric effects. Such screening strongly depends on the vibrational response of the lattice induced by phonons.

Although the MBPT approach may provide enough information about excitonic effects in OILHPs, it will be more interesting when applied to layer type morphologies including exciton–phonon coupling. Hopefully, such simulations will further elaborate the excitonic features with advanced computational methods and machine learning techniques.

2.4.2 Time-dependent density functional theory (TD-DFT) method. Time-dependent density functional theory (TD-DFT)[181–183] is an extended version of DFT. It is specifically designed to describe the excited state properties of materials derived from the frequency dependent linear response function which is helpful in extracting optical spectra and exciton binding energies.[184–186] Based on TD-DFT calculations, Hakamata *et al.* calculated E_{xb} between the photogenerated electron and hole in a 3D cubic 2 × 2 × 2 supercell of $MAPbI_3$. By comparing the electronic excitation energy with the energy difference between the dominant electron and hole states, they found that these values were nearly identical, indicating very weak values for E_{xb} as depicted in Fig. 5(a). The time-averaged E_{xb} was estimated to be 12 ± 9 meV, suggesting that such weakly bound excitons can easily dissociate by thermal energy at RT, leading to freely moving electrons and holes. Fig. 5(b) shows the time evolution of Kohn–Sham eigen energies in non-adiabatic quantum molecular dynamics simulation, with the red and blue curves representing KS energy levels that mainly influence the quasi-electron and quasi-hole, respectively. Here a large number of electronic level crossings can be observed

due to atomic thermal motion, which results in frequent electronic transitions that occur between excited electron and hole states. This *ab initio* study supports the experimental observations and highlights the presence of charge carriers rather than strongly bound excitons in $MAPbI_3$.[187,188]

Similarly, Ganesh *et al.* determined an E_{xb} of 1790 meV for the $MAPbI_3$ cubic structure, which is way too high compared to other theoretical and experimental data. Such a large value can be attributed to using the CAM-B3LYP functional with the LanL2DZ basis set[189] rather than the traditional Perdew–Burke–Ernzerhof (PBE) method involving the plane-wave basis set.[190–192] Gao *et al.*[106] evaluated E_{xb} of 4.88 meV, 5.43 meV, 4.95 meV, and 5.29 meV for 3D $MAPI_3$, $MAPbBr_3$, $FAPbI_3$, and $FAPbBr_3$ respectively. Since E_{xb} defines the amount of separation between electrons and holes, the coulombic interaction between electrons and holes can be calculated as

$$E_{xb} = E_c = \iint \frac{\rho_h(\vec{r}_1)\rho_e(\vec{r}_2)}{|\vec{r}_1 - \vec{r}_2|} d\vec{r}_1 d\vec{r}_2 \quad (16)$$

where ρ_h and ρ_e are hole and electron densities with their coordinates $\vec{r}_1$ and $\vec{r}_2$ respectively. Using the inter-fragment charge transfer method (IFCT),[193,194] the number of electrons transferred can be calculated from the ground state to the first singlet state between each species of perovskites. However, eqn (16) neglects the kinetic energy term associated with electron–hole confinement that highly affects the dielectric behavior.

In addition to bulk OILHPs, Athanasios *et al.* using the simplified TD-DFT method studied the excitonic optical properties of quantum dot (QD) nanostructures. They modeled cuboid QD structures of $MAPbI_3$ and $MAPbBr_3$ each having the size of approximately 1.0–1.5 nm, revealing E_{xb} of 540 meV and 610 meV. These values were significantly larger in the QD regime compared to their bulk counterparts, showcasing the quantum confinement effect. However, these calculations did not account for temperature variations and optical phonon modes which could influence E_{xb}, exciton dynamics and photocarrier lifetimes.

3. Exciton generation, dynamics and recombination

Some researchers also revealed the generation of photoinduced free charge carriers in OILHPs.[187,188,195] The tera-hertz (THz) spectroscopy technique is used to investigate the photoinduced carrier dynamics and its interactions with phonons, which directly affect the exciton population in OILHPs.[196–198] When examining the kinetics of photoinduced charge carriers, Cooke and coworkers,[59] through the analysis of frequency-dependent THz complex conductivity, found that excitons in the form of free charge carriers vanish in perovskite single crystals within 1 ps. This results in a short-lived intra-excitonic transition accompanied by an E_{xb} of 17 meV at RT under high pump fluence. Therefore, in comparison to the recombination process and charge transport, the generation rate of carriers in perovskites is substantially higher. A similar study by Douhal *et al.*[60] found that, a large number of excitons will instantly dissociate into free carriers for the $FAPbI_3$ film. Major findings from their THz analysis revealed that most of the mobile charge carrier population was formed within ~1 ps comparable to the resolution in the THz spectroscopy setup. Jha *et al.*[61] used ultrafast 2D electronic spectroscopy to provide a more direct observation of ultrafast exciton dissociation. The authors demonstrated that excitons spontaneously turn into free carriers in less than 50 fs for the $MAPbI_3$ thin film, which was one of the key reasons for the high efficiency of perovskite photovoltaics.

The correlation between free charge carriers and exciton population after photoinduction under certain equilibrium conditions was also studied.[148,199,200] The coexistence of mobile charge carriers and exciton population at equilibrium can be described by the Saha–Langmuir expression (also known as mass law for excitons and free charges).[201] According to this model, the branching ratio ϕ of the exciton population to free charge carriers can be formulated as

$$\frac{\phi^2}{1-\phi} = \frac{1}{N}\left(\frac{2\pi\mu k_B T}{h^2}\right)^{3/2} \exp\left(-\frac{E_{xb}}{k_B T}\right) \quad (17)$$

where N represents the total number of excitons and free charge

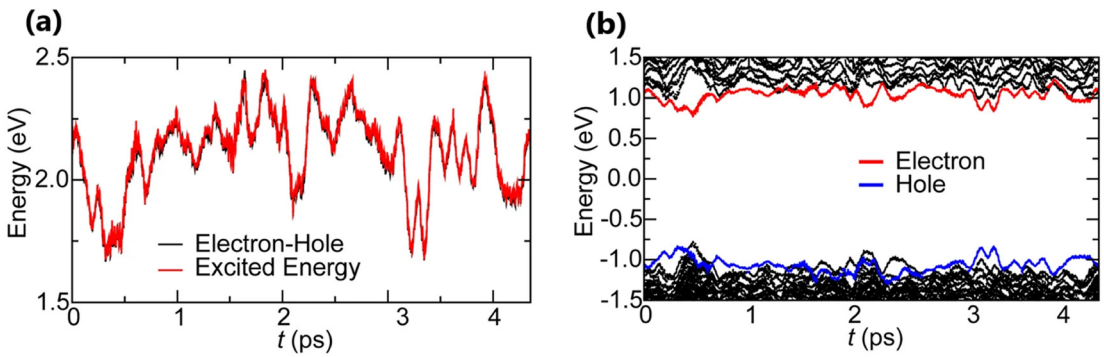

Fig. 5 (a) Time evolution of the many-body electronic excitation energy, including excitonic binding (red), in a 2 × 2 × 2 supercell nonadiabatic quantum molecular dynamics (NAQMD) simulation, along with compared energy difference between the electron and hole (black). (b) Time evolution of KS eigen energies, with the KS states that mostly contribute to the quasi-electron and quasi-hole shown in red and blue, respectively. Adapted from ref. 85, Copyright 2016, Springer Nature.

carriers. D'Innocenzo *et al.* applied this relationship for the first time in perovskites to investigate the equilibrium branching ratio between excitons and free carriers.[148] Using the Saha–Langmuir model Geng *et al.*[202] estimated the E_{xb} of the $FAPbBr_3$ thin film for various excitation densities at RT [Fig. 6(a)]. For higher values of E_{xb}, the dissociation of excitons into free carriers becomes less efficient in perovskites which strongly agrees with the simulations. Furthermore, in the low excitation regions, the fraction of free carriers falls rapidly with increasing exciton population. The exciton to free carrier transition becomes more prevalent for higher excitation regions due to the presence of excited carriers that instantly screen the electrostatic interaction between e–h pairs. Using the data from Fig. 6(a), it is possible to calculate exciton and free carrier densities as a function of fluence [Fig. 6(b)]. According to the Saha-Langmuir relation, the ratio of free charge carriers to excitons increases with temperature; however, it decreases due to the free e–h capture events that are more likely to occur at higher excitation densities.[148]

At certain excitation density (known as critical excitation) at which excitons are completely transformed into free carriers, the Saha–Langmuir relation becomes less relevant. Therefore, the recombination mechanism and excitonic transport are significantly important to evaluate the exciton binding energy. For such a situation, Ulatowski *et al.*[110] investigated charge carrier transport and recombination in various temperature-dependent compositions for OILHPs using a combination of microwave conductivity (at high-frequency) and PL measurements as shown in Fig. 7(a). To simulate the photogenerated conductivity and transient luminescence, a set of rate equations was was used to describe the transport properties of photoinduced charge carriers. Many other authors have also used this method to reveal the behavior of trapping and recombination processes in OILHPs, as shown schematically in Fig. 7(b).[167,203–206]

To study the recombination mechanism, the time evolution of conduction band electron density (n) and trapped electron density (n_T) in a photoinduced pure semiconductor can be described by the following pair of differential equations:

$$\frac{\partial n}{\partial t} = -k_{Bi}np - k_M n - k_T n \quad (18a)$$

$$\frac{\partial n_T}{\partial t} = k_T np - k_E n_T p \quad (18b)$$

where k_{Bi}, k_M, k_T, and k_E are the band-to-band bimolecular, single molecular, trap-mediated, and carrier mediated recombination rate constants respectively. p is the free hole density in the valence band which is the sum of n and n_T. In terms of temperature dependence, the overall patterns of the prompt PL and bimolecular recombination rate for $MAPbI_3$ are shown in Fig. 7(c)–(e) after ref. 110. The bimolecular band-to-band recombination increases for the $MAPbI_3$ thin film as the temperature decreases, showing a narrowing of the thermal distributions of electrons and holes in the valence and conduction bands. The structural phase transition in $MAPbI_3$ instantly affects the behavior of photoinduced charge carriers. At lower temperatures, a funneling of charge carriers will enhance the radiative recombination due to the rise in local charge carrier density. This will rapidly increase both the prompt photoluminescence and the bimolecular recombination rate constant as the temperature is reduced below 150 K [Fig. 7(c)]. At extremely low excitation density and low temperatures, most of the emission takes place at the bandedge due to charge carrier recombination, which was previously believed to be a direct transition from the conduction band to the valence band.[168,207] As obvious in time-integrated PL spectra [Fig. 7(d)], traps with a wide energetic distribution appeared just below the band states. High energy recombination between the conduction band and the valence band dominates the emission spectra at high excitation densities, causing the band tail states to become saturated. With the increase in temperature, the bimolecular recombination rate

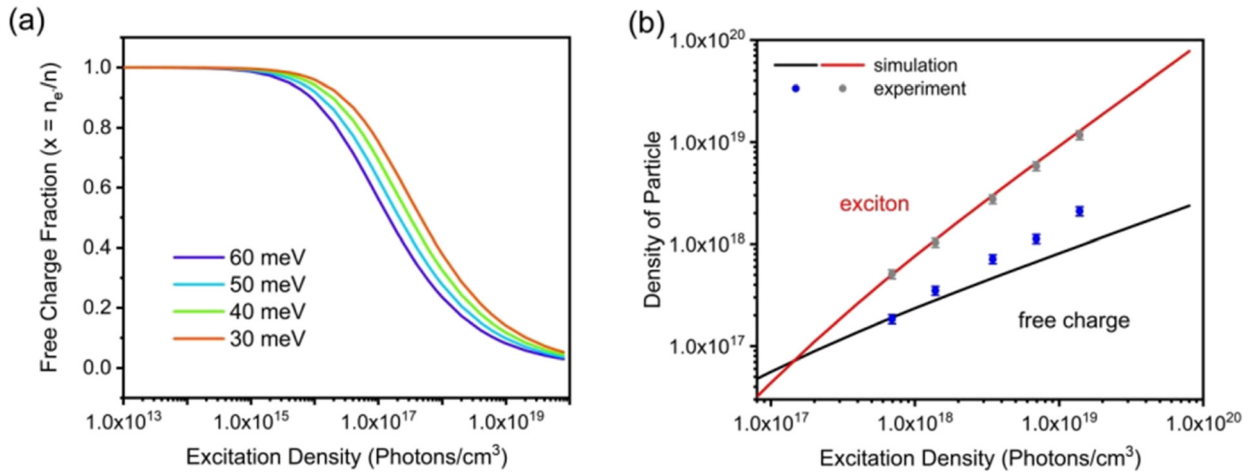

Fig. 6 (a) Modeling of photoexcited free charge carriers in the $FAPbBr_3$ film using different excitation densities according to the Saha–Langmuir equation. E_{xb} = 60, 50, 40, and 30 meV were used with a reduced mass of exciton $\mu = 0.15m_0$. (b) Simulation data were obtained by multiplying the fractions of free charge carriers by the excitation density, and experimental data for free charge carrier and exciton densities were obtained from PL_{max}. Reprinted with permission,[202] Copyright 2023, Springer Royal Society of Chemistry.

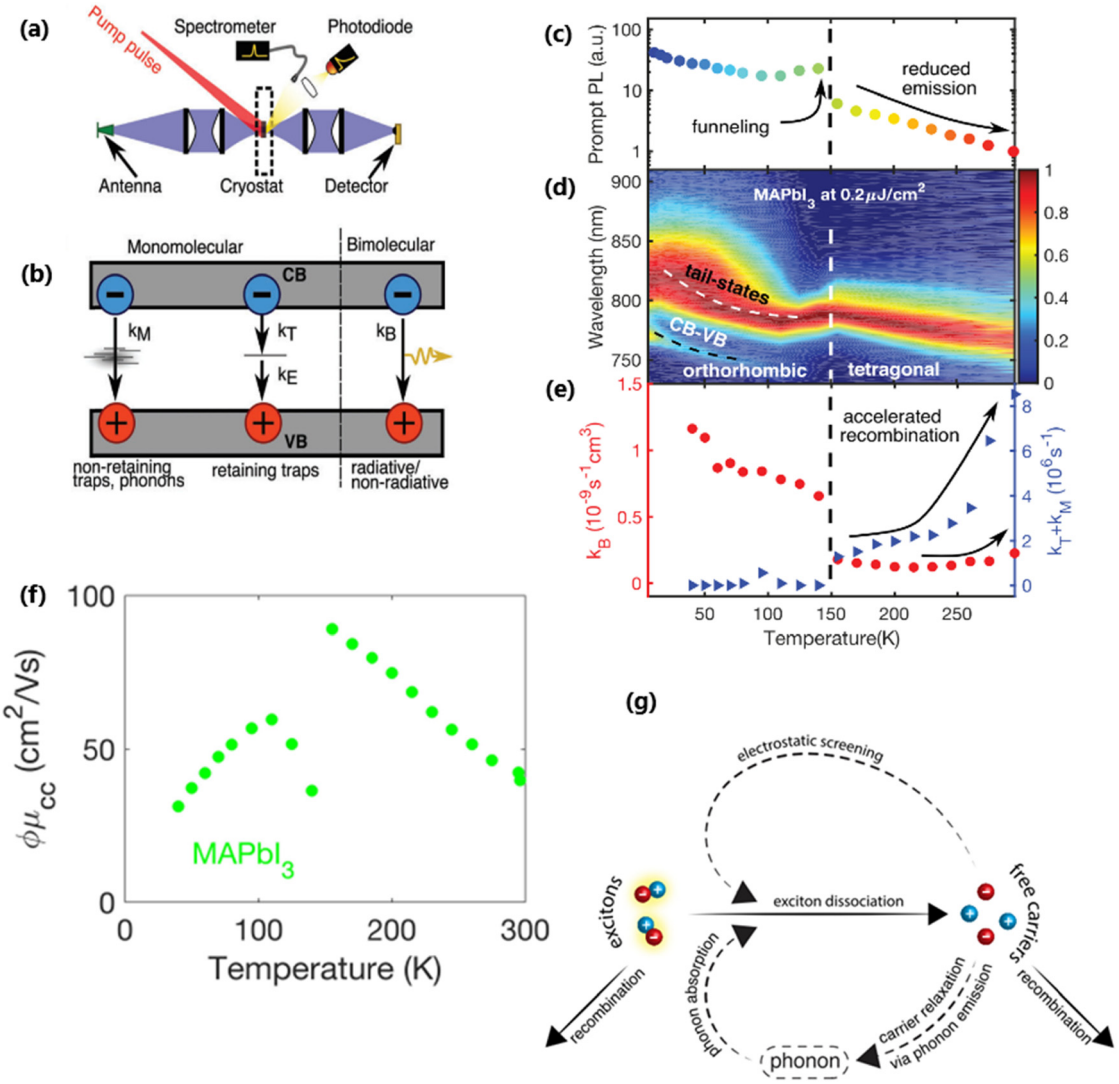

Fig. 7 (a) A schematic experimental setup to obtain data for TRPL and PL spectra. The microwave radiation is launched through the feed horn antenna. The data for PL measurements are obtained through a spectrometer and photodiode. Microwave radiation is detected using a Schottky diode. (b) A simplified model illustrating the mechanism of charge carrier recombination in OILHPs that defines the pathways for both single molecular and bimolecular recombination and distinguishes between charge non-retaining (phonons) and retaining traps. k_M, k_T and k_E represent single molecular, trap-mediated, and carrier mediated recombination rate constants respectively. (c) Prompt PL intensity, (d) emission spectrum, and (e) rates of dynamic decay as a function of temperature, with the dashed line at 150 K representing the phase transition for the $MAPbI_3$ thin film. (f) Temperature-dependent effective charge carrier mobility for the $MAPbI_3$ thin film. Adapted from ref. 110, Copyright 2023, John Wiley & Sons, Inc. (g) Schematic representation of exciton dissociation *via* free carriers, Coulomb screening, and phonons ensuring an enhanced lifetime of free-carrier population. Reprinted with permission,[196] Copyright 2019, American Chemical Society.

constant between the bands slightly increases [Fig. 7(e)]. This increase is accompanied by a much notable increase in the total single molecular trap-mediated recombination constant. This indicates the presence of non-radiative trap-assisted Auger recombination. Moreover, for the low fluence, long wavelength, sub-bandgap emission dominates the spectra below 150 K. The reduced charge carrier mobility in the lower temperature range as shown in Fig. 7(f) indicates that charge carriers localize in energetic traps just below the bandedge which reduces the total charge carrier conductivity of the photoexcited material. At this stage, the exciton generation becomes more prominent as the branching ratio ϕ of photon-to-free-carrier decreases thus reducing the overall charge carrier mobility $\phi\mu_{cc}$. However, for high excitation fluence, the higher energy band-to-band transition becomes the main radiative recombination pathway which produces narrow emission linewidths due to the suppression of electron–phonon coupling.

In the context of exciton–phonon correlation, Fig. 7(g) illustrates the interacting excitons, free carriers, and phonons. Upon photoexcitation, excitons and free carriers are generated, gaining enough kinetic energy to produce a large number of hot phonons as the carriers cool down. The reabsorption of these hot phonons causes excitons to split up into free charge carriers. Meanwhile, the photoinduced free charge carriers

enhance the Coulomb screening, thereby reducing the exciton binding energy which results in even more generation of free charge carriers by exciton dissociation. Such regeneration of free charge carriers due to exciton–phonon interaction and enhanced Coulomb screening are responsible for an extended lifetime of the free charge carrier population in OILHPs.

4. Interplay of polarons

The inclusion of polaronic effects in exciton binding energy measurements is presently an area of active development. Polarons are quasiparticles coupled with the polarization field of the local lattice due to the electron–phonon Coulomb interaction. Such electron–phonon interaction is usually found in polar and ionic semiconductors resulting from the coupling of electronic and longitudinal optical phonon modes. The strength of electron–phonon interaction is higher for systems with larger ionicity. In a perovskite lattice, an injected charge carrier can cause structural distortion of the soft nature of the metal-halide sublattice and reorientation of the polar organic cations to minimize the local lattice's Gibbs free energy. This results in the formation of a spatially extended polarized charge distribution that follows the carrier as it propagates. Depending on the spatial size of the polarized charge distribution, polarons are characterized as small or large polarons. The formation of large polarons results from the long-range electrostatic interactions of the ionic lattice with the free carrier, whereas small polarons are associated with modifications in local bonding. Small polarons are approximately close to one single lattice constant, whereas large polarons are close to numerous unit cells.[208] The phenomena of exciton self-trapping and the resulting low carrier mobility are typically linked to electron–phonon Coulomb interactions that are considered to be primary components governing the carrier transport nature.[62] Moreover, the large polaron formation in the OILHP layer yields higher dielectric constants and screens e–h Coulomb interactions leading to a low recombination rate.[71] Such polaron generation also reduces exciton binding energy and enhances the lifetime and effective masses of the carriers.[63,64] Owing to the formation of large polarons in OILHPs, many attempts have already been made to address some of the unclear optically excited carrier dynamics in these materials. For instance, the discrepancy between long diffusion lengths and relatively moderate carrier mobility can somehow be explained based on large polaron formation despite having small carrier effective mass.[209–211] In the context of exciton binding energy measurement, polaronic effects play a significant role while analyzing the exciton spectrum.[158]

Since in polar systems the majority of carrier interactions take place in the direction of the polarizing field of electrons, the longitudinal optical (LO) phonons produced strongly contribute to the bandedge states than the transverse optical (TO) phonons.[212] The strength of such interactions can be described by a dimensionless quantity known as the Fröhlich coupling constant α[213] given by

$$\alpha = \frac{e^2}{\hbar}\left(\frac{1}{\varepsilon_\infty} - \frac{1}{\varepsilon_0}\right)\sqrt{\frac{m_b}{2E_{LO}}} \tag{19}$$

Here e is the elementary charge, $\hbar$ is the reduced Plank's constant, m_b is the bare effective mass of the electron or hole, and E_{LO} is the LO phonon energy. The terms ε_∞ and ε_0 are the high-frequency dielectric and static dielectric constants respectively and their difference describes ionic screening parameter $1/\varepsilon^*$. In fact, the different values for ε_∞ and ε_0 indicate the electric polarization due to the electron–phonon and optical phonon interactions. In polar semiconductors, the large difference between ε_∞ and ε_0 provides clear evidence for large polaron formation in perovskites, thus renormalizing the carrier effective mass and bandgap energy along with nonhydrogenic exciton states. In a weak coupling regime, the polaron effective mass m_p (in units of m_0) and radius l_p can be approximated as

$$m_p = m_b\left(1 + \frac{\alpha}{6}\right) \tag{20}$$

$$l_p = \sqrt{\frac{\hbar^2 m_b}{E_{LO}}} \tag{21}$$

The results obtained for the above polaron parameters using various experimental and theoretical techniques are summarized in Table 2. The polaronic effects increase the effective mass of the carriers, which results in a decrease in their mobility. According to Evan[214] the increased localizability of the heavy atom causes a more complete screening of its charge by the lattice, which increases the reduced mass. The parameters for polaron effective mass must be treated in terms of the kinetic energy of the Hamiltonian.

4.1 Polaron–exciton models

Various models have been suggested in the literature to explain the role of polarons in exciton binding energy calculations.[223–225] The effective Hamiltonian for a system of excitons interacting with the LO phonon can be expressed as

$$\mathcal{H} = \mathcal{H}_{ex} + \mathcal{H}_{ph} + \mathcal{H}_{ex-ph} \tag{22}$$

The first term includes kinetic energies of carriers and Coulomb interaction given by

$$\mathcal{H}_{ex} = \frac{P^2}{2M} + \frac{p^2}{2\mu} - \frac{e^2}{R\varepsilon_\infty} \tag{23}$$

where P and M refer to momentum and mass of the center-of-mass system, while p and μ represent their relative quantities. $\mathbf{R}$ is the position coordinate. Similarly the Hamiltonian due to phonons can be described as

$$\mathcal{H}_{ph} = \sum_n \frac{P_n^2}{2m_n} + V(\mathbf{R}) \tag{24}$$

Here P_n and m_n are the momentum and mass of the nth system. $V(\mathbf{R})$ is the interacting potential as a function of position $\mathbf{R}$. According to the Haken model[223] the effective interacting potential due to electron–hole Coulomb interaction can be expressed as follows:

$$V(\mathbf{R}) = -\frac{e^2}{\varepsilon_0 R} - \frac{e^2}{\varepsilon_0 R}\left(\frac{1}{\varepsilon_\infty} - \frac{1}{\varepsilon_0}\right)\left(e^{-\mathbf{R}/l_e} + e^{-\mathbf{R}/l_h}\right) \tag{25}$$

Table 2 Parameters for the polaron model using different techniques

Material	Sample morphology	α	m_b (m_0)	m_p (m_0)	ε_0	ε_∞	E_{LO} (meV)	Technique	Ref.
$MAPbI_3$	3D cubic	2.3	0.19	0.263[c]	30	6	8	DFPT(T = 0 K)/MD(T = 300 K) method	Bokdam *et al.*[86]
	Polycrystalline grains	~2.64–2.46	0.1	0.144–0.141	30	5.5	4.84–4.91[a]	Time resolved THz spectroscopy	Jin *et al.*[217]
	3D cubic	2.39	0.12	0.168	24.1	4.5	9.3[a]	DFT + Feynman polaron model	Frost[211]
	Thin films (266 nm)	1.71	0.104[d]	0.134[c]	33.5	5.0	4.96[a]	Far-infrared spectroscopy	Sendner *et al.*[209]
	3D orthorhombic phase	1.18	0.190	0.228	22.54[e]	5.32[f]	3.38[b]	DFT + Pollmann–Büttner model	Proupin *et al.*[158]
	3D orthorhombic phase	1.4	0.22	0.27	—	—	13	DFT+GW and multiphonon Fröhlich model	Schlipf *et al.*[218]
	Thin film	1.91	0.211	0.47	22.6	5.9	12.6	DFPT+GW calculations	Poncé *et al.*[219]
	3D cubic	1.49	0.21	1.20	30.42	6.75	8.76[a]	DFT and Fröhlich's mesoscopic model	Basera *et al.*[108]
	—	1.41	0.23[g]	0.284[c]	19.6[g]	5[g]	19.42	Elliott's band fluctuation (EBF) model	Lizárraga *et al.*[220]
	Single crystal	1.12	0.102	0.114	15	7	12	Magneto-optical spectroscopy and Bajaj exciton-polaron model	Baranowski *et al.*[221]
$MAPbBr_3$	Thin films (287 nm)	1.69	0.117[d]	1.35	32.3	4.7	6.32[a]	Far-infrared spectroscopy	Sendner *et al.*[209]
	—	1.90	0.29	0.382[c]	25.5	4.4	19.97	Elliott's band fluctuation (EBF) model	Lizárraga *et al.*[220]
	3D tetragonal	1.54	0.13	0.16[c]	21.36	4.4	4.10[a]	Time-resolved optical Kerr effect (TR-OKE) spectroscopy and DFT	Miyata *et al.*[222]
	Single crystal	1.75	0.151	0.137	16	5.2	15	Magneto-optical spectroscopy and Bajaj exciton-polaron model	Baranowski *et al.*[221]
$FAPbI_3$	3D cubic	1.37	0.195	1.19	37.91	7.02	9.94[a]	DFT and Fröhlich's mesoscopic model	Basera *et al.*[108]
$FA_{0.85}Cs_{0.15}Pb(I_{0.97}Br_{0.03})_3$	Thin film	3.8	—	0.2	—	—	14.3[a]	Time-resolved terahertz spectroscopy and transient absorption spectroscopy	Bao *et al.*[64]

[a] Frequencies are converted to energy (meV). [b] Cube root result. [c] These values are extracted using eqn (20). [d] Ref. 88. [e] Ref. 215. [f] Ref. 216. [g] Ref. 159.

where $l_{e,h}$ represents electron– and hole–polaron radii as defined according to eqn (21). This theory describes two polaron interactions, each of which has a radius substantially less than the effective radius of excitons. Later, Bajaj[224] proposed a phenomenological modification to the Haken potential to address the overestimation of exciton binding energy in polar crystals:

$$V(\mathbf{R}) = -\frac{e^2}{\varepsilon_0 R} - \frac{e^2}{\varepsilon_0 R}\left(\frac{1}{\varepsilon_\infty} - \frac{1}{\varepsilon_0}\right)\left(e^{-\mathbf{R}/l_e} + e^{-\mathbf{R}/l_h}\right)\left(\frac{\varepsilon_\infty}{\varepsilon_0}\right)^{\gamma} \quad (26)$$

where $\gamma = \frac{3}{5}$ represents the optimal choice for polar crystals having large α values.[224] Pollman and Büttner[225] introduced the electron–polaron and hole–polaron correlations in the Haken potential and the resulting potential can be expressed as

$$V(\mathbf{R}) = -\frac{e^2}{\varepsilon_s R} - \frac{e^2}{\varepsilon_0 R}\left(\frac{1}{\varepsilon_\infty} - \frac{1}{\varepsilon_0}\right)\left(\frac{m_h}{m_h - m_e}e^{-\mathbf{R}/l_h} - \frac{m_e}{m_h - m_e}e^{-\mathbf{R}/l_e}\right) \quad (27)$$

To approximate this potential, it was assumed that the polaron lengths were much smaller than the effective radius of the exciton. This effective radius can be used as an initial input parameter in the variational calculations. Similarly, the exciton–phonon Hamiltonian is given by

$$\mathcal{H}_{ex-ph} = \sum_n V(\mathbf{R}) \quad (28)$$

For a two-particle system, a path integral approach can be followed to study the effects arising due to exciton–phonon interaction. According to these approximations, Park *et al.*[226] evaluated the exciton binding energy of $MAPbI_3$ using static (50.4 meV), dynamic (36.9 meV), and non-local (38.1 meV) screening models. The smaller values of E_{xb} under dynamic and non-local screenings indicate the polaronic effects and the results are consistent with the computed carrier lifetimes and trap-assisted bimolecular e–h recombination rates. Moreover, for a low temperature regime, an E_{xb} of 20.8 meV is obtained for $MAPbI_3$ showing good agreement with experiments.[88,148]

4.2 Polaron formation time

Polaron formation time in OILHPs is highly influenced by both the size of organic cations and vibrational modes of the PbX_3 sublattice.[222,227,228] Such factors affect the energetics of the relevant coupling between organic and inorganic lattices that can provide information about polaron photoexcitation in OILHPs.[229–231] For example, for $MAPbBr_3$ single crystals, Miyata *et al.*[222] using the tight-binding (TB) model reported that the deformation of the $PbBr_3$ sublattice is dominantly responsible for large polaron formation based on the computed small polaron formation time of 0.3 ps for $MAPbBr_3$ in comparison to 0.7 ps for $CsPbBr_3$. The dynamic disorders produced by fluctuations of cations and anions lead to a complex potential energy surface that screens the e–h pair into their corresponding polarons, resulting in a considerable reduction in charge carrier recombination as well as reduced carrier mobility.

A recent study conducted by Bao *et al.*[64] showed strong evidence of polaron formation in $FA_{0.85}Cs_{0.15}Pb(I_{0.97}Br_{0.03})_3$

using the data from their transient absorption spectroscopy (TAS) and time-resolved terahertz spectroscopy (TRTS). The carrier effective mass was calculated with respect to pump–probe delay τ as shown in Fig. 8. After 1 ps, the value of m^* rapidly increased after photoexcitation, indicating that the electron is strongly dressed by its surroundings, and m^* reached a maximum at about 200 ps [Fig. 8(a)]. The persistence of m^* for such a long time can be associated with polaron formation. Here the calculation of m^* was tested using different fitting models to validate m^* estimation [Fig. 8(b)]. However, using the same approach for $MAPbI_3$, m^* peaks were found at 20 ps.

4.3 Polaronic effects from magneto-optical studies

The concept of polaronic effects successfully explains the discrepancies in the optical response, *e.g.*, the rare observation of excited excitonic states, which deviate from the Wannier–Mott exciton model.[115,232,233] It also unveils the considerable differences in the values of the carrier mass reported from magneto-optical studies conducted in high[88,234] and low[235] magnetic field regimes. Baranowski *et al.*[221] employed magneto-optical spectroscopy combined with exciton–polaron modeling to probe carrier–phonon interactions. High-quality perovskite single crystals, including $MAPbI_3$, $MAPbBr_3$, and $CsPbBr_3$, were investigated using ~90 T pulsed magnetic fields. Spectral analysis revealed notable differences in excitonic transition behaviors and effective masses under varying magnetic field strengths. Fig. 9(a) presents the reflection spectrum of $MAPbBr_3$ at 2 K (blue line) alongside its derivative (yellow line), where the minima indicate the energies of excitonic transitions. The optical response is predominantly characterized by a strong 1s excitonic transition at 2.249 eV. A weaker 2s exciton state follows this on the higher energy side at 2.262 eV. The 2s transition strength is significantly smaller than 1/8 of the 1s transition strength, suggesting the polaronic nature of the observed excitonic transition. The reduced effective mass was probed by analyzing the evolution of exciton and Landau level transitions under high magnetic fields. Fig. 9(b) shows the evolution of the reflection spectrum of $MAPbBr_3$. The excitonic states exhibit Zeeman splitting at higher magnetic fields, and both excitonic transitions show a blue shift. The transitions between interband Landau levels are shown in Fig. 9(c) by dividing the spectra measured at nonzero magnetic fields by the spectrum obtained at zero magnetic field. Fig. 9(d)–(f) describes the evolution of the interband Landau level transitions, which are characterized by evenly spaced patterns in the high energy region of the spectrum. This behavior can be well described by the parabolic band dispersion relation:[156]

$$E_{\mathrm{LLn}} = E_{\mathrm{g}} + \left(n + \frac{1}{2}\right)\hbar\omega_{\mathrm{c}} \tag{29}$$

This formula provides direct measurement of the reduced mass of the carriers, yielding values of $0.096m_0$, $0.106m_0$, and $0.117m_0$ for $MAPbI_3$, $MAPbBr_3$, and $CsPbBr_3$ respectively. Such findings reveal that the effective mass of charge carriers, as inferred from Landau level transitions at high fields, was consistently lower compared to the values derived from exciton spectroscopy at low fields, indicating a significant polaronic enhancement. For determining the reduced mass of the carriers in the low field, 1s and 2s excitonic transitions can be used which are detectable irrespective of the field strength. Fig. 9(g)–(i) represents the evolution in the magnetic field shown by diamond points. Observing 1s and 2s excitonic states simultaneously constrains the exciton binding energy, leaving just the reduced effective mass, μ, as a fitting parameter. The dashed red lines show that the Wannier–Mott model reasonably describes the shifts of the 1s and 2s states due to the applied magnetic field, as well as their energy separation. However, the data fitting requires significantly higher μ values than those obtained from Landau level observations at high magnetic fields. This shows that excitons act differently than those predicted by Landau level analysis, which depends on bare carrier mass. This finding strongly indicates polaronic mass enhancement in OILHPs. The use of bare carrier masses, as predicted by the Wannier–Mott-exciton model, fails to fit the data, as illustrated by the short-dashed red lines.

Shin *et al.*[236] explored the magneto-photoluminescence transitions in single crystals of $MAPbX_3$ (X = Cl, Br, and I) subjected to strong magnetic fields of ~60 T at 4.2 K.

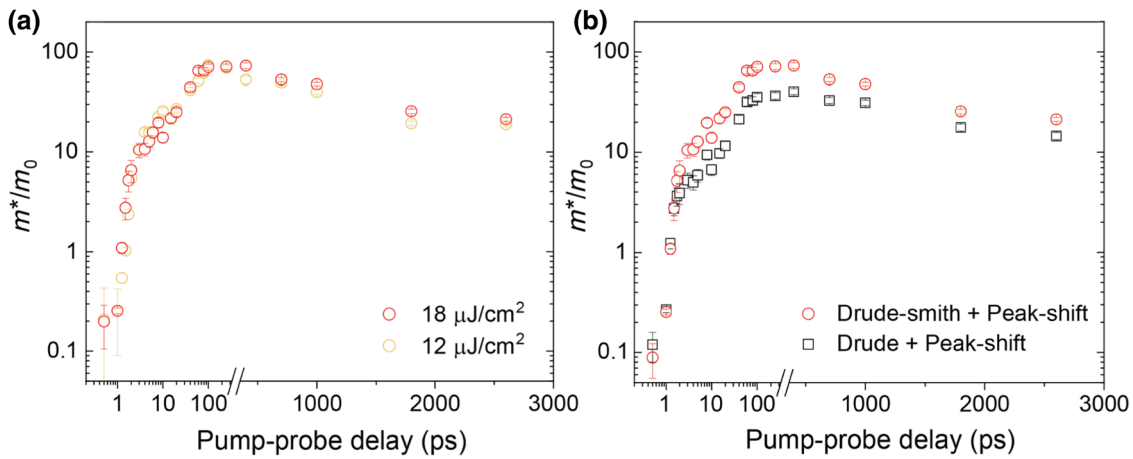

Fig. 8 (a) Effective mass of electrons as a function of pump–probe delay using the Drude-Smith + peak-shift formulation for various fluence intensities. (b) Comparison of the Drude-Smith + peak-shift and Drude + peak-shift formulation for calculation of the effective mass of electrons. Adapted from ref. 64, Copyright 2023, American Physical Society.

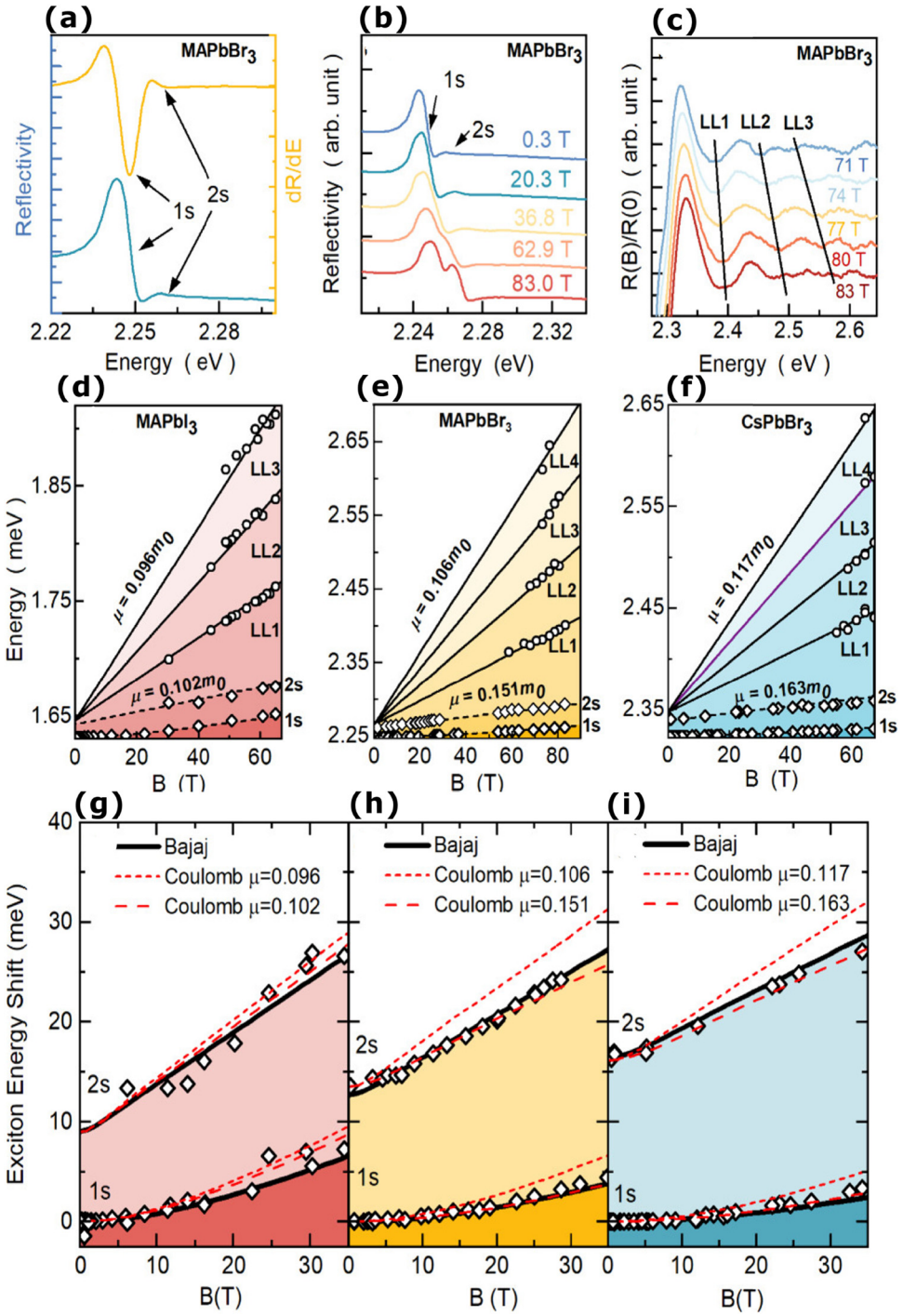

Fig. 9 (a) The reflectance spectrum of $MAPbBr_3$ with the corresponding derivative (yellow) displaying resonance characteristics of the excitonic transitions 1s and 2s. (b) The evolution of the reflectance spectrum in the magnetic field. (c) Rationed reflectance spectra for various values of the magnetic field strengths; the black lines correspond to transitions of the Landau level (LL). (d)–(f) Fan charts illustrating the energies for Landau level interband transition for $MAPbI_3$, $MAPbBr_3$, and $CsPbBr_3$ with respect to magnetic field strength. Effective reduced mass μ was evaluated using eqn (29). (g)–(i) Energies of 1s and 2s excitonic transitions for $MAPbI_3$, $MAPbBr_3$, and $CsPbBr_3$ with respect to magnetic field strength (open points). The red dashed line represents the Wannier–Mott theory, while the red short-dashed line represents a prediction of the Wannier–Mott theory with μ obtained from the spectroscopy of the Landau level. The black line corresponds to the Bajaj potential. Adapted from ref. 221, Copyright 2024, American Chemical Society.

Photoluminescence spectra were recorded under varying magnetic field strengths, revealing a power-law dependence of shifts in transition energy for both σ^+ and σ^- directions in $MAPbI_3$. Their study showed that the combination of polaronic effects and Rashba splitting can explain the photoluminescence transitions generated by the various halogens under magnetic fields, which are difficult to describe by a single unified model. Such findings underscore the need to

incorporate polaronic effects into models of perovskite materials to accurately predict their optical and electronic properties, thereby advancing their application in optoelectronic devices.

Here we have discussed some aspects of polaron formation and its impact on optical response and carrier effective masses in OILHPs, but it still lacks which method can surely be universally suitable for thin films as well as bulk cube-like structures. The theories of Haken and Pollman–Büttner satisfactorily explain the excitons and polarons in OILHPs at low temperatures where excitonic effects are much more prominent but will be more challenging for higher temperature phases where such effects practically disappear due to the increase in static dielectric associated with the rotational motion and steric effects of organic cations.[128,237] Understanding polarons in such systems requires improved experimental and theoretical techniques capable of exploring both excitonic and polaronic properties at the bulk and nanoscale. More emphasis should be placed on polaron formation, dynamics, dielectric and quantum confinement effects, and their relation to carrier scattering, and dielectric properties, for different morphologies. Therefore, a careful analysis of these factors needs to be undertaken to conclude the universal method for evaluating the exciton binding energy along with the polaron formation mechanism in OILHPs which is critical for the designing and fabrication of photovoltaic as well as optoelectronic devices.

5. Summary and outlook

In this article, an adequate understanding of excitonic and polaronic physics in OILHPs is presented. The exciton binding energy (E_{xb}) of various OILHPs with different morphologies and compositions has been measured at different temperatures using both experimental and theoretical techniques. Some of the factors that lead to conflicting values for exciton binding energy by different authors in OILHPs can be summarized as follows. Most of the calculated exciton binding energy is based on the Wannier–Mott model which raises serious concerns about the accuracy of whether to use the static or high frequency dielectric constant. In the previous literature, it was assumed that E_{xb} is independent of the magnetic field and that the use of the high frequency dielectric constant may yield results with high uncertainties. The E_{xb} in OILHPs is evaluated using the static dielectric constant, which replaces the effective dielectric constant during calculations. While this method is useful, it is only applicable when the exciton binding energy is lower than the longitudinal optical phonon energy.[72] Ambient conditions, such as temperature and pressure, greatly influence absorption and photoluminescence spectra, affecting the vibrational modes of atoms and lattice dynamics. This, in turn, leads to different recombination and coupling mechanisms of photogenerated carriers, resulting in a wide range of E_{xb}. Crystal quality, morphology and trap states also influence the screening behavior of the photogenerated charge carriers, which alters the bimolecular and trap-assisted recombination processes, which in turn affects the excitonic properties in OILHPs. It is also evident that complexities arise in low dimensional OILHPs like 2D thin films, nanostructures, or quantum dots stemming from quantum confinement and modified dielectric confinement, which demand distinct approaches.

The role of large polaron formation in OILHPs is presently under intense debate. Considering polaron formation and its correlation to carrier recombination mechanisms, carrier effective mass and mobility can somewhat explain the discrepancies in calculating the exciton binding energy. However, it will be interesting to explore the polaron dynamics and carrier scattering upon photoexcitation in bulk and layered form of OILHPs using single experimental or theoretical techniques to provide a universal image for excitonic and polaronic physics (beyond the dielectric and quantum confinement effects). This will address the existing discrepancies in the excitonic and polaronic behavior of OILHPs in their optically excited state, and provide a clearer understanding of their impact on photovoltaic and optoelectronic properties.

Author contributions

Zeeshan Muhammad: investigation and writing – original draft, Arooj Rashid: writing – original draft.

Data availability

There are no raw data related to this review paper.

Conflicts of interest

The authors affirm that they have no known financial or interpersonal issues that would have appeared to have an impact on the research described in this publication.

References

1 J. H. Noh, S. H. Im, J. H. Heo, T. N. Mandal and S. I. Seok, *Nano Lett.*, 2013, **13**, 1764–1769.
2 F. Hao, C. C. Stoumpos, R. P. H. Chang and M. G. Kanatzidis, *J. Am. Chem. Soc.*, 2014, **136**, 8094–8099.
3 W. Rehman, R. L. Milot, G. E. Eperon, C. Wehrenfennig, J. L. Boland, H. J. Snaith, M. B. Johnston and L. M. Herz, *Adv. Mater.*, 2015, **27**, 7938–7944.
4 D. Bi, W. Tress, M. I. Dar, P. Gao, J. Luo, C. Renevier, K. Schenk, A. Abate, F. Giordano, J. P. Correa Baena, J. D. Decoppet, S. M. Zakeeruddin, M. K. Nazeeruddin, M. Grätzel and A. Hagfeldt, *Sci. Adv.*, 2016, **2**, e1501170.
5 L. Li, N. Liu, Z. Xu, Q. Chen, X. Wang and H. Zhou, *ACS Nano*, 2017, **11**, 8804–8813.
6 K. A. Bush, K. Frohna, R. Prasanna, R. E. Beal, T. Leijtens, S. A. Swifter and M. D. McGehee, *ACS Energy Lett.*, 2018, **3**, 428–435.
7 E. S. Parrott, T. Green, R. L. Milot, M. B. Johnston, H. J. Snaith and L. M. Herz, *Adv. Funct. Mater.*, 2018, **28**, 1802803.

8 Y. Chen, H. T. Yi, X. Wu, R. Haroldson, Y. N. Gartstein, Y. I. Rodionov, K. S. Tikhonov, A. Zakhidov, X. Y. Zhu and V. Podzorov, *Nat. Commun.*, 2016, **7**, 12253.
9 A. A. Zhumekenov, M. I. Saidaminov, M. A. Haque, E. Alarousu, S. P. Sarmah, B. Murali, I. Dursun, X.-H. Miao, A. L. Abdelhady, T. Wu, O. F. Mohammed and O. M. Bakr, *ACS Energy Lett.*, 2016, **1**, 32–37.
10 G. Xing, N. Mathews, S. Sun, S. S. Lim, Y. M. Lam, M. Gratzel, S. Mhaisalkar and T. C. Sum, *Science*, 2013, **342**, 344–347.
11 G. W. P. P. Adhyaksa, L. W. Veldhuizen, Y. Kuang, S. Brittman, R. E. I. I. Schropp and E. C. Garnett, *Chem. Mater.*, 2016, **28**, 5259–5263.
12 C. Wehrenfennig, G. E. Eperon, M. B. Johnston, H. J. Snaith and L. M. Herz, *Adv. Mater.*, 2014, **26**, 1584–1589.
13 J. Lim, M. T. Hörantner, N. Sakai, J. M. Ball, S. Mahesh, N. K. Noel, Y. H. Lin, J. B. Patel, D. P. McMeekin, M. B. Johnston, B. Wenger and H. J. Snaith, *Energy Environ. Sci.*, 2019, **12**, 169–176.
14 N. T. P. Hartono, S. Sun, M. C. Gélvez-Rueda, P. J. Pierone, M. P. Erodici, J. Yoo, F. Wei, M. Bawendi, F. C. Grozema, M. J. Sher, T. Buonassisi and J.-P. P. Correa-Baena, *J. Mater. Chem. A*, 2019, **7**, 23949–23957.
15 T. M. Brenner, D. A. Egger, L. Kronik, G. Hodes and D. Cahen, *Nat. Rev. Mater.*, 2016, **1**, 15007.
16 T. Leijtens, G. E. Eperon, A. J. Barker, G. Grancini, W. Zhang, J. M. Ball, A. R. S. Kandada, H. J. Snaith and A. Petrozza, *Energy Environ. Sci.*, 2016, **9**, 3472–3481.
17 H. T. Yi, X. Wu, X. Zhu and V. Podzorov, *Adv. Mater.*, 2016, **28**, 6509–6514.
18 N. Arora, M. I. Dar, M. Hezam, W. Tress, G. Jacopin, T. Moehl, P. Gao, A. S. Aldwayyan, B. Deveaud, M. Grätzel and M. K. Nazeeruddin, *Adv. Funct. Mater.*, 2016, **26**, 2846–2854.
19 J. Shi, Y. Li, J. Wu, H. Wu, Y. Luo, D. Li, J. J. Jasieniak and Q. Meng, *Appl. Phys.*, arXiv.
20 P. Brenner, O. Bar-On, M. Jakoby, I. Allegro, B. S. Richards, U. W. Paetzold, I. A. Howard, J. Scheuer and U. Lemmer, *Nat. Commun.*, 2019, **10**, 988.
21 P. Liu, C. Gu and Q. Liao, *ACS Omega*, 2021, **6**, 34021–34026.
22 T. Shen, J. Qin, Y. Bai, J. Zhang, L. Shi, X. Hou, J. Zi and B. Hu, *Opto-Electron. Adv.*, 2022, **5**, 200051.
23 H. Kim, L. Zhao, J. S. Price, A. J. Grede, K. Roh, A. N. Brigeman, M. Lopez, B. P. Rand and N. C. Giebink, *Nat. Commun.*, 2018, **9**, 4893.
24 Y. Shang, Y. Liao, Q. Wei, Z. Wang, B. Xiang, Y. Ke, W. Liu and Z. Ning, *Sci. Adv.*, 2019, **5**, eaaw8072.
25 A. S. Pannu, S. Sen, X. (Tony) Wang, R. Jones, K. (Ken) Ostrikov and P. Sonar, *Nanoscale*, 2023, **15**, 2659–2666.
26 L. Dou, Y. Yang, J. You, Z. Hong, W.-H. Chang, G. Li and Y. Yang, *Nat. Commun.*, 2014, **5**, 5404.
27 C. Xie, C. Liu, H. Loi and F. Yan, *Adv. Funct. Mater.*, 2020, **30**, 1903907.
28 Y. Yang, H. Dai, F. Yang, Y. Zhang, D. Luo, X. Zhang, K. Wang, X. W. Sun and J. Yao, *Nanoscale Res. Lett.*, 2019, **14**, 291.
29 R. Ray, N. Nakka and S. K. Pal, *Nanotechnology*, 2021, **32**, 085201.
30 I.-H. Park, K. C. Kwon, Z. Zhu, X. Wu, R. Li, Q.-H. Xu and K. P. Loh, *J. Am. Chem. Soc.*, 2020, **142**, 18592–18598.
31 L. Mei, R. Huang, C. Shen, J. Hu, P. Wang, Z. Xu, Z. Huang and L. Zhu, *Adv. Opt. Mater.*, 2022, **10**, 2102656.
32 A. Moeini, L. Martínez-Sarti, K. P. S. Zanoni, M. Sessolo, D. Tordera and H. J. Bolink, *J. Mater. Chem. C*, 2022, **10**, 13878–13885.
33 M. B. Mohammadzadeh Shamloo, S. Darbari and Y. Abdi, in 2021 Iranian International Conference on Microelectronics (IICM), IEEE, 2021, pp. 1–4.
34 Y. Xu, F. Wang, J. Xu, X. Lv, G. Zhao, Z. Sun, Z. Xie and S. Zhu, *Opt. Express*, 2023, **31**, 8428.
35 J. Fan, B. Jia and M. Gu, *Photonics Res.*, 2014, **2**, 111.
36 M. Szafrański and A. Katrusiak, *J. Phys. Chem. Lett.*, 2017, **8**, 2496–2506.
37 L. K. Jagadamma, O. Blaszczyk, M. T. Sajjad, A. Ruseckas and I. D. W. Samuel, *Sol. Energy Mater. Sol. Cells*, 2019, **201**, 110071.
38 G. Grancini and M. K. Nazeeruddin, *Nat. Rev. Mater.*, 2018, **4**, 4–22.
39 Y. Furukawa, S. Ikawa, H. Kiyohara, Y. Sendai and A. Bahtiar, *Key Eng. Mater.*, 2020, **860**, 3–8.
40 A.-B. Mekky, *Ann. Chim. - Sci. des Matériaux*, 2020, **44**, 179–184.
41 M. L. Ball, J. V. Milić and Y.-L. Loo, *Chem. Mater.*, 2022, **34**, 2495–2502.
42 A. Olaleru, E. Maluta, J. Kirui and O. Adekoya, *Thin Films Photovoltaics*, IntechOpen, 2022.
43 A. Bulloch, S. Wang, P. Ghosh and L. K. Jagadamma, *Philos. Trans. R. Soc., A.*, 2022, **380**, 20210144.
44 M. Saba, F. Quochi, A. Mura and G. Bongiovanni, *Acc. Chem. Res.*, 2016, **49**, 166–173.
45 S. A. Kulkarni, S. G. Mhaisalkar, N. Mathews and P. P. Boix, *Small Methods*, 2019, **3**, 1–16.
46 N. Droseros, D. Tsokkou and N. Banerji, *Adv. Energy Mater.*, 2020, **10**, 1903258.
47 W. Gao, J. Ding, Z. Bai, Y. Qi, Y. Wang and Z. Lv, *Nanophotonics*, 2021, **10**, 3945–3955.
48 M. Li, P. Huang and H. Zhong, *J. Phys. Chem. Lett.*, 2023, **14**, 1592–1603.
49 D. E. Hill, *Solid State Commun.*, 1972, **11**, 1187–1191.
50 W. J. Turner, W. E. Reese and G. D. Pettit, *Phys. Rev.*, 1964, **136**, A1467–A1470.
51 A. Sugie, K. Nakano, K. Tajima, I. Osaka and H. Yoshida, *J. Phys. Chem. Lett.*, 2023, **14**, 11412–11420.
52 Y. Zhu, F. Zhao, W. Wang, Y. Li, S. Zhang and Y. Lin, *Adv. Energy Sustainability Res.*, 2022, **3**, 2100184.
53 B. Schweitzer and H. Bässler, *Synth. Met.*, 2000, **109**, 1–6.
54 M. Liess, S. Jeglinski, Z. V. Vardeny, M. Ozaki, K. Yoshino, Y. Ding and T. Barton, *Phys. Rev. B: Condens. Matter Mater. Phys.*, 1997, **56**, 15712–15724.
55 J.-L. Brédas, D. Beljonne, V. Coropceanu and J. Cornil, *Chem. Rev.*, 2004, **104**, 4971–5004.
56 A. Bian, D. He, S. Hao, Y. Fu, L. Zhang, J. He, Y. Wang and H. Zhao, *Nanoscale*, 2020, **12**, 8485–8492.

57 M. E. Ziffer, J. C. Mohammed and D. S. Ginger, *ACS Photonics*, 2016, **3**, 1060–1068.
58 S. Parveen, K. K. Paul, R. Das and P. K. Giri, *J. Colloid Interface Sci.*, 2019, **539**, 619–633.
59 D. A. Valverde-Chávez, C. S. Ponseca, C. C. Stoumpos, A. Yartsev, M. G. Kanatzidis, V. Sundström and D. G. Cooke, *Energy Environ. Sci.*, 2015, **8**, 3700–3707.
60 P. Piatkowski, B. Cohen, C. S. Ponseca, M. Salado, S. Kazim, S. Ahmad, V. Sundström and A. Douhal, *J. Phys. Chem. Lett.*, 2016, **7**, 204–210.
61 A. Jha, H.-G. Duan, V. Tiwari, P. K. Nayak, H. J. Snaith, M. Thorwart and R. J. D. Miller, *ACS Photonics*, 2018, **5**, 852–860.
62 W. P. D. Wong, J. Yin, B. Chaudhary, X. Y. Chin, D. Cortecchia, S.-Z. A. Lo, A. C. Grimsdale, O. F. Mohammed, G. Lanzani and C. Soci, *ACS Mater. Lett.*, 2020, **2**, 20–27.
63 Y. Park and D. T. Limmer, *J. Chem. Phys.*, 2022, **157**, 11780.
64 D. Bao, Q. Chang, B. Chen, X. Chen, H. Sun, Y. M. Lam, D. Zhao, J.-X. Zhu and E. E. M. Chia, *PRX Energy*, 2023, **2**, 013001.
65 H. Haug and S. W. Koch, *Quantum Theory of the Optical and Electronic Properties of Semiconductors*, World Scientific, 5th edn, 2009.
66 G. H. Wannier, *Phys. Rev.*, 1937, **52**, 191–197.
67 G. Dresselhaus, *J. Phys. Chem. Solids*, 1956, **1**, 14–22.
68 A. Poglitsch and D. Weber, *J. Chem. Phys.*, 1987, **87**, 6373–6378.
69 N. Onoda-Yamamuro, T. Matsuo and H. Suga, *J. Phys. Chem. Solids*, 1992, **53**, 935–939.
70 Q. Lin, A. Armin, R. C. R. Nagiri, P. L. Burn and P. Meredith, *Nat. Photonics*, 2015, **9**, 106–112.
71 E. J. Juarez-Perez, R. S. Sanchez, L. Badia, G. Garcia-Belmonte, Y. S. Kang, I. Mora-Sero and J. Bisquert, *J. Phys. Chem. Lett.*, 2014, **5**, 2390–2394.
72 H. Kalt and C. F. Klingshirn, *Semiconductor Optics 1*, Springer International Publishing, Cham, 5th edn, 2019.
73 M. Hirasawa, T. Ishihara, T. Goto, K. Uchida and N. Miura, *Phys. B*, 1994, **201**, 427–430.
74 T. Ishihara, *J. Lumin.*, 1994, **60–61**, 269–274.
75 T. J. Savenije, C. S. Ponseca, L. Kunneman, M. Abdellah, K. Zheng, Y. Tian, Q. Zhu, S. E. Canton, I. G. Scheblykin, T. Pullerits, A. Yartsev and V. Sundström, *J. Phys. Chem. Lett.*, 2014, **5**, 2189–2194.
76 I. B. Koutselas, L. Ducasse and G. C. Papavassiliou, *J. Phys.: Condens. Matter*, 1996, **8**, 1217–1227.
77 S. Sun, T. Salim, N. Mathews, M. Duchamp, C. Boothroyd, G. Xing, T. C. Sum and Y. M. Lam, *Energy Environ. Sci.*, 2014, **7**, 399–407.
78 K. Tanaka, T. Takahashi, T. Ban, T. Kondo, K. Uchida and N. Miura, *Solid State Commun.*, 2003, **127**, 619–623.
79 M. Saba, M. Cadelano, D. Marongiu, F. Chen, V. Sarritzu, N. Sestu, C. Figus, M. Aresti, R. Piras, A. Geddo Lehmann, C. Cannas, A. Musinu, F. Quochi, A. Mura and G. Bongiovanni, *Nat. Commun.*, 2014, **5**, 5049.
80 G. Grancini, A. R. Srimath Kandada, J. M. Frost, A. J. Barker, M. De Bastiani, M. Gandini, S. Marras, G. Lanzani, A. Walsh and A. Petrozza, *Nat. Photonics*, 2015, **9**, 695–701.
81 M. A. Green, Y. Jiang, A. M. Soufiani and A. Ho-Baillie, *J. Phys. Chem. Lett.*, 2015, **6**, 4774–4785.
82 A. Kumar, N. K. Kumawat, P. Maheshwari and D. Kabra, in 2015 IEEE 42nd Photovoltaic Specialist Conference (PVSC), IEEE, 2015, pp. 1–4.
83 Y. Yamada, T. Nakamura, M. Endo, A. Wakamiya and Y. Kanemitsu, *IEEE J. Photovoltaics*, 2015, **5**, 401–405.
84 Y. Yang, M. Yang, Z. Li, R. Crisp, K. Zhu and M. C. Beard, *J. Phys. Chem. Lett.*, 2015, **6**, 4688–4692.
85 T. Hakamata, K. Shimamura, F. Shimojo, R. K. Kalia, A. Nakano and P. Vashishta, *Sci. Rep.*, 2016, **6**, 19599.
86 M. Bokdam, T. Sander, A. Stroppa, S. Picozzi, D. D. Sarma, C. Franchini and G. Kresse, *Sci. Rep.*, 2016, **6**, 28618.
87 S. A. March, C. Clegg, D. B. Riley, D. Webber, I. G. Hill and K. C. Hall, *Sci. Rep.*, 2016, **6**, 1–7.
88 K. Galkowski, A. Mitioglu, A. Miyata, P. Plochocka, O. Portugall, G. E. Eperon, J. T.-W. W. Wang, T. Stergiopoulos, S. D. Stranks, H. J. Snaith and R. J. Nicholas, *Energy Environ. Sci.*, 2016, **9**, 962–970.
89 H. Zheng, J. Dai, J. Duan, F. Chen, G. Zhu, F. Wang and C. Xu, *J. Mater. Chem. C*, 2017, **5**, 12057–12061.
90 T. Ye, M. Petrovic, S. Peng, J. L. K. Yoong, C. Vijila and S. Ramakrishna, *ACS Appl. Mater. Interfaces*, 2017, **9**, 2358–2368.
91 F. Ruf, A. Magin, M. Schultes, E. Ahlswede, H. Kalt and M. Hetterich, *Appl. Phys. Lett.*, 2018, **112**, 083902.
92 J. Shi, H. Zhang, Y. Li, J. J. Jasieniak, Y. Li, H. Wu, Y. Luo, D. Li and Q. Meng, *Energy Environ. Sci.*, 2018, **11**, 1460–1469.
93 C. L. Davies, M. R. Filip, J. B. Patel, T. W. Crothers, C. Verdi, A. D. Wright, R. L. Milot, F. Giustino, M. B. Johnston and L. M. Herz, *Nat. Commun.*, 2018, **9**, 1–9.
94 A. Koliogiorgos, C. S. Garoufalis, I. Galanakis and S. Baskoutas, *ACS Omega*, 2018, **3**, 18917–18924.
95 P. Umari, E. Mosconi and F. De Angelis, *J. Phys. Chem. Lett.*, 2018, **9**, 620–627.
96 Y. Liu, J. Wang, N. Zhu, W. Liu, C. Wu, C. Liu, L. Xiao, Z. Chen and S. Wang, *Opt. Lett.*, 2019, **44**, 3474.
97 F. Ruf, M. F. Aygüler, N. Giesbrecht, B. Rendenbach, A. Magin, P. Docampo, H. Kalt and M. Hetterich, *APL Mater.*, 2019, **7**, 031113.
98 Z. W. Xu, C. R. Zhang, Y. Z. Wu, J. J. Gong, W. Wang, Z. J. Liu and H. S. Chen, *Results Phys.*, 2019, **15**, 102709.
99 Q. Xu, A. Stroppa, J. Lv, X. Zhao, D. Yang, K. Biswas and L. Zhang, *Phys. Rev. Mater.*, 2019, **3**, 125401.
100 Y. Bai, H. Zhang, M. Zhang, D. Wang, H. Zeng, J. Zhao, H. Xue, G. Wu, J. Su, Y. Xie, Y. Zhang, H. Jing, H. Yu, Z. Hu, R. Peng, M. Wang and Y. Wu, *Nanoscale*, 2020, **12**, 1100–1108.
101 M. Hamada, S. Rana, E. Jokar, K. Awasthi, E. W. G. Diau and N. Ohta, *ACS Appl. Energy Mater.*, 2020, **3**, 11830–11840.
102 R. Ali, Z. G. Zhu, Q. B. Yan, Q. R. Zheng, G. Su, A. Laref, C. S. Saraj and C. Guo, *ACS Appl. Mater. Interfaces*, 2020, **12**, 49636–49647.

103 C. Xiong, J. Sun, C. Cai, W. Caiyang and Y. Zhu, *Sol. Energy*, 2020, **204**, 155–160.
104 D. Li, D. Li, H. Zhang, A. Yang and C. Liang, *J. Phys. Chem. Lett.*, 2020, **11**, 5282–5294.
105 A. Simbula, R. Pau, Q. Wang, F. Liu, V. Sarritzu, S. Lai, M. Lodde, F. Mattana, G. Mula, A. Geddo Lehmann, I. D. Spanopoulos, M. G. Kanatzidis, D. Marongiu, F. Quochi, M. Saba, A. Mura and G. Bongiovanni, *Adv. Opt. Mater.*, 2021, **9**, 2100295.
106 Z. Gao, S. Chen, Y. Bai, M. Wang, X. Liu, W. Yang, W. Li, X. Ding and J. Yao, *Phys. Chem. Chem. Phys.*, 2021, **23**, 11548–11556.
107 C. C. S. Chan, K. Fan, H. Wang, Z. Huang, D. Novko, K. Yan, J. Xu, W. C. H. Choy, I. Lončarić and K. S. Wong, *Adv. Energy Mater.*, 2021, **11**, 2003071.
108 P. Basera, A. Singh, D. Gill and S. Bhattacharya, *J. Mater. Chem. C*, 2021, **9**, 17113–17123.
109 G. Biffi, Y. Cho, R. Krahne and T. C. Berkelbach, *J. Phys. Chem. C*, 2023, **127**, 1891–1898.
110 A. M. Ulatowski, K. A. Elmestekawy, J. B. Patel, N. K. Noel, S. Yan, H. Kraus, P. G. Huggard, M. B. Johnston and L. M. Herz, *Adv. Funct. Mater.*, 2023, 2305283.
111 F. Zhang, H. Zhong, C. Chen, X. G. Wu, X. Hu, H. Huang, J. Han, B. Zou and Y. Dong, *ACS Nano*, 2015, **9**, 4533–4542.
112 K. Zheng, Q. Zhu, M. Abdellah, M. E. Messing, W. Zhang, A. Generalov, Y. Niu, L. Ribaud, S. E. Canton and T. Pullerits, *J. Phys. Chem. Lett.*, 2015, **6**, 2969–2975.
113 H. Kunugita, T. Hashimoto, Y. Kiyota, Y. Udagawa, Y. Takeoka, Y. Nakamura, J. Sano, T. Matsushita, T. Kondo, T. Miyasaka and K. Ema, *Chem. Lett.*, 2015, **44**, 852–854.
114 J. Dai, H. Zheng, C. Zhu, J. Lu and C. Xu, *J. Mater. Chem. C*, 2016, **4**, 4408–4413.
115 J. Tilchin, D. N. Dirin, G. I. Maikov, A. Sashchiuk, M. V. Kovalenko and E. Lifshitz, *ACS Nano*, 2016, **10**, 6363–6371.
116 H. Kunugita, Y. Kiyota, Y. Udagawa, Y. Takeoka, Y. Nakamura, J. Sano, T. Matsushita, T. Kondo and K. Ema, *Jpn. J. Appl. Phys.*, 2016, **55**, 060304.
117 T. Thu Ha Do, A. Granados Del Águila, C. Cui, J. Xing, Z. Ning and Q. Xiong, *Phys. Rev. B*, 2017, **96**, 1–9.
118 Z. Liu, Y. Li, X. Guan, Y. Mi, A. Al-Hussain, S. T. Ha, M. H. Chiu, C. Ma, M. R. Amer, L. J. Li, J. Liu, Q. Xiong, J. Wang, X. Liu and T. Wu, *J. Phys. Chem. Lett.*, 2019, **10**, 2363–2371.
119 J. Shi, Y. Li, J. Wu, H. Wu, Y. Luo, D. Li, J. J. Jasieniak and Q. Meng, *Adv. Opt. Mater.*, 2020, **8**, 1–11.
120 A. M. Ulatowski, A. D. Wright, B. Wenger, L. R. V. Buizza, S. G. Motti, H. J. Eggimann, K. J. Savill, J. Borchert, H. J. Snaith, M. B. Johnston and L. M. Herz, *J. Phys. Chem. Lett.*, 2020, **11**, 3681–3688.
121 M. Jain, D. Gill, P. Bhumla, P. Basera and S. Bhattacharya, *Appl. Phys. Lett.*, 2021, **118**, 192103.
122 S. Yan, K. Wang, G. Xing, J. Xu, S. Su, Z. Tang, S. Wang and K. W. Ng, *ACS Appl. Mater. Interfaces*, 2021, **13**, 38458–38466.
123 H.-H. Fang, F. Wang, S. Adjokatse, N. Zhao, J. Even and M. Antonietta Loi, *Light: Sci. Appl.*, 2016, **5**, e16056.
124 F. Yuan, Z. Wu, H. Dong, J. Xi, K. Xi, G. Divitini, B. Jiao, X. Hou, S. Wang and Q. Gong, *J. Phys. Chem. C*, 2017, **121**, 15318–15325.
125 A. V. Sachenko, V. P. Kostylyov, A. V. Bobyl, V. M. Vlasyuk, I. O. Sokolovskyi, E. I. Terukov and M. A. Evstigneev, *Tech. Phys. Lett.*, 2017, **43**, 678–680.
126 Y. Fu, T. Wu, J. Wang, J. Zhai, M. J. Shearer, Y. Zhao, R. J. Hamers, E. Kan, K. Deng, X. Y. Zhu and S. Jin, *Nano Lett.*, 2017, **17**, 4405–4414.
127 C. L. Davies, J. Borchert, C. Q. Xia, R. L. Milot, H. Kraus, M. B. Johnston and L. M. Herz, *J. Phys. Chem. Lett.*, 2018, **9**, 4502–4511.
128 A. Johnston, G. Walters, M. I. Saidaminov, Z. Huang, K. Bertens, N. Jalarvo and E. H. Sargent, *ACS Nano*, 2020, **14**, 15107–15118.
129 Z. Muhammad, P. Liu, R. Ahmad, S. Jalali-Asadabadi, C. Franchini and I. Ahmad, *AIP Adv.*, 2022, **12**, 025330.
130 N. J. Jeon, J. Seo, S. Nah and J.-K. Lee, *Adv. Chem. Eng. Sci.*, 2022, **12**, 54–64.
131 S. Wang, Q. Zhao, A. Hazarika, S. Li, Y. Wu, Y. Zhai, X. Chen, J. M. Luther and G. Li, *Nat. Commun.*, 2023, **14**, 2216.
132 K. A. Elmestekawy, B. M. Gallant, A. D. Wright, P. Holzhey, N. K. Noel, M. B. Johnston, H. J. Snaith and L. M. Herz, *ACS Energy Lett.*, 2023, 2543–2551.
133 A. Perumal, S. Shendre, M. Li, Y. K. E. Tay, V. K. Sharma, S. Chen, Z. Wei, Q. Liu, Y. Gao, P. J. S. Buenconsejo, S. T. Tan, C. L. Gan, Q. Xiong, T. C. Sum and H. V. Demir, *Sci. Rep.*, 2016, **6**, 36733.
134 L. Yang, K. Wei, Z. Xu, F. Li, R. Chen, X. Zheng, X. Cheng and T. Jiang, *Opt. Lett.*, 2018, **43**, 122.
135 D. Han, M. Imran, M. Zhang, S. Chang, X. G. Wu, X. Zhang, J. Tang, M. Wang, S. Ali, X. Li, G. Yu, J. Han, L. Wang, B. Zou and H. Zhong, *ACS Nano*, 2018, **12**, 8808–8816.
136 H. Fang, W. Deng, X. Zhang, X. Xu, M. Zhang, J. Jie and X. Zhang, *Nano Res.*, 2019, **12**, 171–176.
137 Z. Liu, Z. Hu, Z. Zhang, J. Du, J. Yang, X. Tang, W. Liu and Y. Leng, *ACS Photonics*, 2019, **6**, 3150–3158.
138 F. Meng, X. Liu, Y. Chen, X. Cai, M. Li, T. Shi, Z. Chen, D. Chen, H. L. Yip, C. Ramanan, P. W. M. Blom and S. J. Su, *Adv. Funct. Mater.*, 2020, **30**, 1–9.
139 L. Sui, G. Niu, J. Jiang, Q. Li, Y. Zhang, G. Wu, F. Li and K. Yuan, *J. Phys. Chem. C*, 2020, **124**, 14390–14399.
140 J. Liu, F. Hu, Y. Zhou, C. Zhang, X. Wang and M. Xiao, *J. Lumin.*, 2020, **221**, 117032.
141 S. Peng, Z. Wen, T. Ye, X. Xiao, K. Wang, J. Xia, J. Sun, T. Zhang, G. Mei, H. Liu, B. Xu, X. Li, R. Chen, G. Xing, K. Wang and Z. Tang, *ACS Appl. Mater. Interfaces*, 2020, **12**, 31863–31874.
142 X. Wang, Q. Wang, Z. Chai and W. Wu, *RSC Adv.*, 2020, **10**, 44373–44381.
143 X. Li, K. Wang, M. Chen, S. Wang, Y. Fan, T. Liang, Q. Song, G. Xing and Z. Tang, *Adv. Opt. Mater.*, 2020, **8**, 1–7.
144 C. Zhang, S. Wang, X. Li, M. Yuan, L. Turyanska and X. Yang, *Adv. Funct. Mater.*, 2020, **30**, 1910582.
145 S. M. H. Qaid, H. M. Ghaithan, K. K. AlHarbi, A. F. Bin Ajaj, B. A. Al-Asbahi and A. S. Aldwayyan, *Photonics*, 2021, **9**, 4.

146 X. Zhang, S. Xiao, X. Wang, T. He and R. Chen, *Chin. Phys. B*, 2023, **32**, 064212.
147 R. Comin, G. Walters, E. S. Thibau, O. Voznyy, Z. H. Lu and E. H. Sargent, *J. Mater. Chem. C*, 2015, **3**, 8839–8843.
148 V. D. Innocenzo, G. Grancini, M. J. P. P. Alcocer, A. R. S. Kandada, S. D. Stranks, M. M. Lee, G. Lanzani, H. J. Snaith, A. Petrozza, V. D'Innocenzo, G. Grancini, M. J. P. P. Alcocer, A. R. S. Kandada, S. D. Stranks, M. M. Lee, G. Lanzani, H. J. Snaith and A. Petrozza, *Nat. Commun.*, 2014, **5**, 3586.
149 S. Liu, W. Huang, P. Liao, N. Pootrakulchote, H. Li, J. Lu, J. Li, F. Huang, X. Shai, X. Zhao, Y. Shen, Y. B. Cheng and M. Wang, *J. Mater. Chem. A*, 2017, **5**, 22952–22958.
150 K. Awasthi, K.-B. B. Du, C.-Y. Y. Wang, C.-L. L. Tsai, M. Hamada, S. Narra, E. W.-G. G. Diau and N. Ohta, *ACS Photonics*, 2018, **5**, 2408–2417.
151 T. J. Whitcher, J. X. Zhu, X. Chi, H. Hu, D. Zhao, T. C. Asmara, X. Yu, M. B. H. Breese, A. H. Castro Neto, Y. M. Lam, A. T. S. Wee, E. E. M. Chia and A. Rusydi, *Phys. Rev. X*, 2018, **8**, 1–10.
152 H. W. Chen, D. P. Gulo, Y. C. Chao and H. L. Liu, *Sci. Rep.*, 2019, **9**, 1–9.
153 L. D. F. Zhang, X. Zhang, C. Wang, M. Sun, X. Luo, Y. Yang, S. Chang and D. Zhang, *Nano Energy*, 2021, **79**, 105486.
154 N. Rybin, D. Ghosh, J. Tisdale, S. Shrestha, M. Yoho, D. Vo, J. Even, C. Katan, W. Nie, A. J. Neukirch and S. Tretiak, *Chem. Mater.*, 2020, **32**, 1854–1863.
155 Z. Muhammad, P. Liu, R. Ahmad, S. Jalali Asadabadi, C. Franchini and I. Ahmad, *Phys. Chem. Chem. Phys.*, 2020, **22**, 11943–11955.
156 N. Miura, *Physics of Semiconductors in High Magnetic Fields*, Oxford University Press, Oxford, 2007.
157 A. Miyata, A. Mitioglu, P. Plochocka, O. Portugall, J. T.-W. Wang, S. D. Stranks, H. J. Snaith and R. J. Nicholas, *Nat. Phys.*, 2015, **11**, 582–587.
158 E. Menéndez-Proupin, C. L. Beltrán Ríos and P. Wahnón, *Phys. Status Solidi RRL*, 2015, **9**, 559–563.
159 A. M. Soufiani, F. Huang, P. Reece, R. Sheng, A. Ho-Baillie and M. A. Green, *Appl. Phys. Lett.*, 2015, **107**, 231902.
160 P. C. Makado and N. C. McGill, *J. Phys. C: Solid State Phys.*, 1986, **19**, 873–885.
161 Y. Yang, D. P. Ostrowski, R. M. France, K. Zhu, J. Van De Lagemaat, J. M. Luther and M. C. Beard, *Nat. Photonics*, 2016, **10**, 53–59.
162 R. J. Elliott, *Phys. Rev.*, 1957, **108**, 1384–1389.
163 P. Y. Yu and M. Cardona, *Fundamentals of Semiconductors*, Springer Berlin Heidelberg, Berlin, Heidelberg, 3rd edn, 2005.
164 X. Chen, H. Lu, Y. Yang and M. C. Beard, *J. Phys. Chem. Lett.*, 2018, **9**, 2595–2603.
165 N. Sestu, M. Cadelano, V. Sarritzu, F. Chen, D. Marongiu, R. Piras, M. Mainas, F. Quochi, M. Saba, A. Mura and G. Bongiovanni, *J. Phys. Chem. Lett.*, 2015, **6**, 4566–4572.
166 J. Even, L. Pedesseau and C. Katan, *J. Phys. Chem. C*, 2014, **118**, 11566–11572.
167 S. D. Stranks, V. M. Burlakov, T. Leijtens, J. M. Ball, A. Goriely and H. J. Snaith, *Phys. Rev. Appl.*, 2014, **2**, 034007.
168 A. D. Wright, R. L. Milot, G. E. Eperon, H. J. Snaith, M. B. Johnston and L. M. Herz, *Adv. Funct. Mater.*, 2017, **27**, 1700860.
169 F. Bruneval, F. Sottile, V. Olevano, R. Del Sole and L. Reining, *Phys. Rev. Lett.*, 2005, **94**, 186402.
170 G. Strinati, *Phys. Rev. B: Condens. Matter Mater. Phys.*, 1984, **29**, 5718–5726.
171 M. Rohlfing and S. G. Louie, *Phys. Rev. B: Condens. Matter Mater. Phys.*, 2000, **62**, 4927–4944.
172 F. Fuchs, C. Rödl, A. Schleife and F. Bechstedt, *Phys. Rev. B: Condens. Matter Mater. Phys.*, 2008, **78**, 085103.
173 F. Ferreira and R. M. Ribeiro, *Phys. Rev. B*, 2017, **96**, 115431.
174 P. Liu, B. Kim, X. Q. Chen, D. D. Sarma, G. Kresse and C. Franchini, *Phys. Rev. Mater.*, 2018, **2**, 75003.
175 X. Wu, D. Vanderbilt and D. R. Hamann, *Phys. Rev. B: Condens. Matter Mater. Phys.*, 2005, **72**, 035105.
176 M. Gajdoš, K. Hummer, G. Kresse, J. Furthmüller and F. Bechstedt, *Phys. Rev. B: Condens. Matter Mater. Phys.*, 2006, **73**, 045112.
177 M. A. Pérez-Osorio, R. L. Milot, M. R. Filip, J. B. Patel, L. M. Herz, M. B. Johnston and F. Giustino, *J. Phys. Chem. C*, 2015, **119**, 25703–25718.
178 M. Kato, T. Fujiseki, T. Miyadera, T. Sugita, S. Fujimoto, M. Tamakoshi, M. Chikamatsu and H. Fujiwara, *J. Appl. Phys.*, 2017, **121**, 115501.
179 P. F. Ndione, Z. Li and K. Zhu, *J. Mater. Chem. C*, 2016, **4**, 7775–7782.
180 G. Mannino, I. Deretzis, E. Smecca, A. La Magna, A. Alberti, D. Ceratti and D. Cahen, *J. Phys. Chem. Lett.*, 2020, **11**, 2490–2496.
181 E. Runge and E. K. U. Gross, *Phys. Rev. Lett.*, 1984, **52**, 997–1000.
182 M. Petersilka, U. J. Gossmann and E. K. U. Gross, *Phys. Rev. Lett.*, 1996, **76**, 1212–1215.
183 C. A. Ullrich, *Time-Dependent Density-Functional Theory: Concepts and Applications*, Oxford University Press, 2012.
184 S. Botti, F. Sottile, N. Vast, V. Olevano, L. Reining, H.-C. Weissker, A. Rubio, G. Onida, R. Del Sole and R. W. Godby, *Phys. Rev. B: Condens. Matter Mater. Phys.*, 2004, **69**, 155112.
185 Z. Yang and C. A. Ullrich, *Phys. Rev. B: Condens. Matter Mater. Phys.*, 2013, **87**, 195204.
186 Y.-M. Byun and C. A. Ullrich, *Phys. Rev. B*, 2017, **95**, 205136.
187 J. S. Manser and P. V. Kamat, *Nat. Photonics*, 2014, **8**, 737–743.
188 Y. Yamada, T. Nakamura, M. Endo, A. Wakamiya and Y. Kanemitsu, *J. Am. Chem. Soc.*, 2014, **136**, 11610–11613.
189 T. Yanai, D. P. Tew and N. C. Handy, *Chem. Phys. Lett.*, 2004, **393**, 51–57.
190 J. P. Perdew, J. A. Chevary, S. H. Vosko, K. A. Jackson, M. R. Pederson, D. J. Singh and C. Fiolhais, *Phys. Rev. B: Condens. Matter Mater. Phys.*, 1992, **46**, 6671–6687.
191 D. M. Ceperley and B. J. Alder, *Phys. Rev. Lett.*, 1980, **45**, 566–569.
192 P. E. Blöchl, *Phys. Rev. B: Condens. Matter Mater. Phys.*, 1994, **50**, 17953–17979.

193 T. Lu and F. Chen, *J. Comput. Chem.*, 2012, **33**, 580–592.
194 P. Bultinck, C. Van Alsenoy, P. W. Ayers and R. Carbó-Dorca, *J. Chem. Phys.*, 2007, **126**, 144111.
195 Y. Jiang, X. Wang and A. Pan, *Adv. Mater.*, 2019, **31**, 1–47.
196 D. Zhao, H. Hu, R. Haselsberger, R. A. Marcus, M.-E. Michel-Beyerle, Y. M. Lam, J.-X. Zhu, C. La-o-vorakiat, M. C. Beard and E. E. M. Chia, *ACS Nano*, 2019, **13**, 8826–8835.
197 D. Zhao and E. E. M. Chia, *Adv. Opt. Mater.*, 2020, **8**, 1900783.
198 R. L. Milot, G. E. Eperon, H. J. Snaith, M. B. Johnston and L. M. Herz, *Adv. Funct. Mater.*, 2015, **25**, 6218–6227.
199 C. Sheng, C. Zhang, Y. Zhai, K. Mielczarek, W. Wang, W. Ma, A. Zakhidov and Z. V. Vardeny, *Phys. Rev. Lett.*, 2015, **114**, 116601.
200 Y.-C. Hsiao, T. Wu, M. Li, Q. Liu, W. Qin and B. Hu, *J. Mater. Chem. A*, 2015, **3**, 15372–15385.
201 M. N. Saha, *Proceedings of the Royal Society of London. Series A*, Containing Papers of a Mathematical and Physical Character, 1921, vol. 99, pp. 135–153.
202 X. Geng, Y. Liu, X. Zou, E. M. J. Johansson and J. Sá, *Phys. Chem. Chem. Phys.*, 2023, **25**, 22607–22613.
203 E. M. Hutter, G. E. Eperon, S. D. Stranks and T. J. Savenije, *J. Phys. Chem. Lett.*, 2015, **6**, 3082–3090.
204 M. J. Trimpl, A. D. Wright, K. Schutt, L. R. V. Buizza, Z. Wang, M. B. Johnston, H. J. Snaith, P. Müller-Buschbaum and L. M. Herz, *Adv. Funct. Mater.*, 2020, **30**, 2004312.
205 A. Kiligaridis, P. A. Frantsuzov, A. Yangui, S. Seth, J. Li, Q. An, Y. Vaynzof and I. G. Scheblykin, *Nat. Commun.*, 2021, **12**, 3329.
206 E. M. H. Tom, J. Savenije, D. Guo and V. M. Caselli, *Adv. Energy Mater.*, 2020, **10**, 1903788.
207 A. D. Wright, C. Verdi, R. L. Milot, G. E. Eperon, M. A. Pérez-Osorio, H. J. Snaith, F. Giustino, M. B. Johnston and L. M. Herz, *Nat. Commun.*, 2016, **7**, 11755.
208 W. Nie, J.-C. Blancon, A. J. Neukirch, K. Appavoo, H. Tsai, M. Chhowalla, M. A. Alam, M. Y. Sfeir, C. Katan, J. Even, S. Tretiak, J. J. Crochet, G. Gupta and A. D. Mohite, *Nat. Commun.*, 2016, **7**, 11574.
209 M. Sendner, P. K. Nayak, D. A. Egger, S. Beck, C. Müller, B. Epding, W. Kowalsky, L. Kronik, H. J. Snaith, A. Pucci and R. Lovrinčić, *Mater. Horiz.*, 2016, **3**, 613–620.
210 X.-Y. Zhu and V. Podzorov, *J. Phys. Chem. Lett.*, 2015, **6**, 4758–4761.
211 J. M. Frost, *Phys. Rev. B*, 2017, **96**, 195202.
212 A. M. Fox, *Optical Properties of Solids*, Oxford University Press, 2001.
213 H. Fröhlich, *Adv. Phys.*, 1954, **3**, 325–361.
214 E. O. Kane, *Phys. Rev. B: Solid State*, 1978, **18**, 6849–6855.
215 F. Brivio, A. B. Walker and A. Walsh, *APL Mater.*, 2013, **1**, 042111.
216 E. Menéndez-Proupin, P. Palacios, P. Wahnón and J. C. Conesa, *Phys. Rev. B: Condens. Matter Mater. Phys.*, 2014, **90**, 045207.
217 Z. Jin, Y. Peng, Y. Fang, Z. Ye, Z. Fan, Z. Liu, X. Bao, H. Gao, W. Ren, J. Wu, G. Ma, Q. Chen, C. Zhang, A. V. Balakin, A. P. Shkurinov, Y. Zhu and S. Zhuang, *Light: Sci. Appl.*, 2022, **11**, 209.
218 M. Schlipf, S. Poncé and F. Giustino, *Phys. Rev. Lett.*, 2018, **121**, 086402.
219 S. Poncé, M. Schlipf and F. Giustino, *ACS Energy Lett.*, 2019, **4**, 456–463.
220 K. Lizárraga, P. Llontop, L. A. Enrique-Morán, M. Piñeiro, E. Perez, E. Serquen, A. Tejada, F. Ruske, L. Korte and J. A. Guerra, *arXiv*, 2023, preprint, arXiv:2306.17314, DOI: 10.48550/arXiv.2306.17314.
221 M. Baranowski, A. Nowok, K. Galkowski, M. Dyksik, A. Surrente, D. Maude, M. Zacharias, G. Volonakis, S. D. Stranks, J. Even, M. Maczka, R. Nicholas and P. Plochocka, *ACS Energy Lett.*, 2024, **9**, 2696–2702.
222 K. Miyata, D. Meggiolaro, M. T. Trinh, P. P. Joshi, E. Mosconi, S. C. Jones, F. De Angelis and X.-Y. Zhu, *Sci. Adv.*, 2017, **3**, e1701217.
223 H. Haken, *Fortschr. Phys.*, 1958, **6**, 271–334.
224 K. K. Bajaj, *Solid State Commun.*, 1974, **15**, 1221–1224.
225 J. Pollmann and H. Büttner, *Phys. Rev. B: Solid State*, 1977, **16**, 4480–4490.
226 Y. Park, A. Obliger and D. T. Limmer, *Nano Lett.*, 2022, **22**, 2398–2404.
227 H. Uratani and H. Nakai, *J. Phys. Chem. Lett.*, 2020, **11**, 4448–4455.
228 H. Zhu, K. Miyata, Y. Fu, J. Wang, P. P. Joshi, D. Niesner, K. W. Williams, S. Jin and X.-Y. Zhu, *Science*, 2016, **353**, 1409–1413.
229 J. Yang, X. Wen, H. Xia, R. Sheng, Q. Ma, J. Kim, P. Tapping, T. Harada, T. W. Kee, F. Huang, Y.-B. Cheng, M. Green, A. Ho-Baillie, S. Huang, S. Shrestha, R. Patterson and G. Conibeer, *Nat. Commun.*, 2017, **8**, 14120.
230 V. Carpenella, C. Fasolato, D. Di Girolamo, J. Barichello, F. Matteocci, C. Petrillo, D. Dini and A. Nucara, *J. Phys. Chem. C*, 2023, **127**, 22097–22104.
231 D. Meggiolaro, F. Ambrosio, E. Mosconi, A. Mahata and F. De Angelis, *Adv. Energy Mater.*, 2020, **10**, 1902748.
232 M. Baranowski, K. Galkowski, A. Surrente, J. Urban, Ł. Kłopotowski, S. Maćkowski, D. K. Maude, R. Ben Aich, K. Boujdaria, M. Chamarro, C. Testelin, P. K. Nayak, M. Dollmann, H. J. Snaith, R. J. Nicholas and P. Plochocka, *Nano Lett.*, 2019, **19**, 7054–7061.
233 Z. Yang, A. Surrente, K. Galkowski, N. Bruyant, D. K. Maude, A. A. Haghighirad, H. J. Snaith, P. Plochocka and R. J. Nicholas, *J. Phys. Chem. Lett.*, 2017, **8**, 1851–1855.
234 Z. Yang, A. Surrente, K. Galkowski, A. Miyata, O. Portugall, R. J. Sutton, A. A. Haghighirad, H. J. Snaith, D. K. Maude, P. Plochocka and R. J. Nicholas, *ACS Energy Lett.*, 2017, **2**, 1621–1627.
235 Y. Yamada, H. Mino, T. Kawahara, K. Oto, H. Suzuura and Y. Kanemitsu, *Phys. Rev. Lett.*, 2021, **126**, 237401.
236 Y. H. Shin, H. Choi, C. Park, D. Park, M. S. Jeong, H. Nojiri, Z. Yang, Y. Kohama and Y. Kim, *Phys. Rev. B*, 2021, **104**, 035205.
237 J. M. Frost, K. T. Butler and A. Walsh, *APL Mater.*, 2014, **2**, 081506.